Mon. Not. R. astr. Soc. (1992) **256**, 186–208

A study of FRII radio galaxies with $z<0.15$ – I. High-resolution maps of eight sources at 3.6 cm

A. R. S. Black,[1] S. A. Baum,[2] J. P. Leahy,[3] R. A. Perley,[4] J. M. Riley[1] and P. A. G. Scheuer[1]

[1]*Mullard Radio Astronomy Observatory, Cavendish Laboratory, Madingley Road, Cambridge CB3 0HE*
[2]*Space Telescope Science Institute, 3700 San Martin Drive, Baltimore, Maryland, 21218, USA*
[3]*Nuffield Radio Astronomy Laboratories, Jodrell Bank, Macclesfield, Cheshire SK11 9DL*
[4]*National Radio Astronomy Observatory, Very Large Array Program, Socorro, New Mexico, 87801, USA*

Received 1991 November 28. Received 1991 November 25; in original form 1991 October 22

SUMMARY

VLA maps of total intensity and fractional polarization at 3.6 cm are presented for eight radio galaxies, part of a sample of 30 nearby FRII sources with $P_{178}>2\times10^{25}$ W Hz^{-1} sr^{-1}. High-sensitivity images of the hotspots (with resolutions of 0.25 and 0.75 arcsec and average noise levels of ~ 30 μJy) show strikingly different and complex structures. Jets are found in six of the sources.

Key words: galaxies: active – galaxies: jets – radio continuum: galaxies.

1 INTRODUCTION

In the now well-established jet model of extragalactic radio sources (Begelman, Blandford & Rees 1984), a hotspot represents the end of a relativistic jet emanating from the nucleus of a giant elliptical galaxy. Analysis of the hotspots should allow determination of the parameters of the 'feeding' beams and of the enveloping intergalactic medium (IGM), and so inform us of the processes of shock formation and particle acceleration which are at work. Furthermore, the energetics of the radio lobes may be better understood since their constituents must have been processed *through* the hotspots.

Until now, few hotspots have been mapped with sufficient sensitivity and resolution to trace the path of any faint jet into the hotspot and to follow any post-shock flow. Moreover, those mapped in detail [e.g. 3C405 – Carilli, Dreher & Perley (1989), Carilli (1990); 3C33 – Rudnick (1988), Rudnick & Anderson (1990)] show remarkably *dissimilar* structures – even those at opposite ends of the same source. This has inhibited the development even of a classification scheme for the hotspots, let alone any more detailed understanding in terms of the available jet models and numerical simulations (e.g. Scheuer 1981; Williams & Gull 1985; Norman 1989; Cox, Gull & Scheuer 1991).

We have embarked upon a project to map a large sample of FRII radio sources at high resolution using the new low-noise 8-GHz receiver system of the Very Large Array (VLA). The sample, listed in Table 1, consists of 30 FRII (Fanaroff & Riley 1974) sources from the 3CR catalogue with $z<0.15$ and $P_{178}>1.5\times10^{25}$ W Hz^{-1} sr^{-1}. A value for Hubble's constant of $H_0=50$ km s^{-1} Mpc^{-1} and for the deceleration parameter of $q_0=0$ have been assumed throughout. Ten other sources which fulfil these criteria were excluded from this sample since they do not have hotspots characteristic of FRII sources: nine have broad featureless lobes (FRII Fat Doubles, Muxlow & Garrington 1991) and one is a giant radio galaxy.

Six sources in the sample have already been mapped in great detail by others [3C33 – Rudnick (1988), Rudnick & Anderson (1990); 3C277.3 – van Breugel *et al.* (1985); 3C285 – van Breugel, in preparation; 3C303 – Kronberg (1986); 3C321 – van Breugel, in preparation; 3C388 – Burns, Christiansen & Hough (1982); 3C405 – Carilli (1990)] and there are no plans to remap them at present. The remaining 24 sources have been observed at 3.6 cm in B- and C-configurations, and, where appropriate, in A- and D-configurations also. This paper presents VLA maps of eight sources. High-sensitivity ($\overline{\sigma}_{\rm I}\simeq 30$ μJy), high-resolution (average linear resolution $\overline{D}_{\rm FWHM}\simeq 0.7$ kpc) maps are given for regions around the hotspots, together with lower resolution maps of the entire source, so that the hotspots may be considered in context.

In the text, the word 'jet' is used to refer to narrow and extended features of emission, which may or may not be continuous.

Detailed discussion of these sources is deferred to later papers.

2 OBSERVATIONS

All observations were made at frequencies of 8235 and 8465 MHz. The bandwidth ($\Delta\nu$) was usually 50 MHz, except for the larger sources observed in the A- and B-configurations where narrower bandwidths of 25 and 12.5 MHz were necessary.

Table 1. The sample of FRII radio galaxies.

Source	IAU name	z	S_{178} (Jy)	α_{tot}	P_{178}	θ (arcsec)	D (kpc)
3C15	0034–014	0.0730	15.8	0.64	33	47	90
3C33	0106+130	0.0595	54.4	0.76	75	270	430
3C98	0356+102	0.0306	47.2	0.78	17	310	270
3C105	0404+035	0.0890	17.8	0.58	55	340	760
3C111	0415+379	0.0485	64.6	0.73	59	220	280
3C135	0511+008	0.1273	17.3	0.92	120	130	410
3C136.1	0512+248	0.0640	14.0	0.69	22	470	790
3C184.1	0734+805	0.1182	13.0	0.68	73	190	550
3C192	0802+243	0.0598	21.1	0.79	30	210	330
3C197.1	0818+472	0.1301	8.1	0.69	56	18	56
3C198	0819+061	0.0815	9.7	0.69	25	530	1100
3C223	0936+361	0.1368	14.7	0.74	110	310	1000
3C223.1	0938+399	0.1075	6.0	0.56	27	85	230
3C227	0945+076	0.0861	30.4	0.67	89	250	520
3C277.3	1251+278	0.0794	9.0	0.58	26	39	87
3C285	1319+428	0.0857	11.3	0.95	24	180	400
3C303	1441+522	0.1410	11.2	0.76	92	47	160
3C321	1529+242	0.0960	13.5	0.60	49	310	750
3C327	1559+021	0.1039	35.3	0.61	150	290	750
3C353	1717+009	0.0304	236.0	0.71	83	290	250
3C382	1833+326	0.0578	19.9	0.59	26	190	290
3C388	1842+455	0.0908	24.6	0.70	81	43	100
3C390.3	1845+797	0.0569	47.5	0.75	60	240	360
3C403	1949+023	0.0590	17.8	0.45	24	110	170
3C405	1957+405	0.0565	8700	0.74	11000	130	190
3C424	2045+068	0.1270	14.6	0.85	98	33	100
3C430	2117+605	0.0541	33.7	0.72	40	90	130
3C433	2121+248	0.1016	56.2	0.75	230	58	150
3C445	2221+394	0.0562	24.8	0.85	31	600	910
3C452	2243+394	0.0811	54.4	0.78	140	280	590

Column 4 gives the flux densities at 178 MHz and column 5 the spectral index from Spinrad *et al.* (1985). Column 6 gives the radio power calculated from the corrected (Laing *et al.* 1983; 1.09×) fluxes of column 4 in units of 10^{24} W Hz^{-1} sr^{-1}. Column 7 lists the angular extent of detected emission along the main axis of the source and column 8 the linear equivalent. The eight sources in bold are those for which maps are presented in this paper.

For all of the 24 sources, B- and C-configuration data were collected. The B-maps were examined to determine if the hotspots showed any *unresolved* detail with sufficient surface brightness to merit A-observations: eight fields of view were found to be suitable. For most sources, D-data were acquired. A log of the observations is given in Table 2.

For nine of the more extended sources, data were collected with the pointing centre located at each end of the source separately. This was necessary because at large displacements from the pointing centre (≥ 100 arcsec) the loss in sensitivity of the primary beam ($\theta_{\rm FWHM}^{\rm primary} \simeq 300$ arcsec at 8.3 GHz) and the effects of bandwidth and time-average smearing become important. Such observations are denoted by P (preceding) and F (following). Despite this precaution, in A- and sometimes B-configurations it was still necessary to reduce the bandwidth for these sources – observation times were increased accordingly, to achieve the same limiting sensitivity. Table 3 gives observational details for each source.

Table 2. Log of VLA observations for the entire project.

Date	Config	τ_{obs}^{tot} (hr)
1990 May 24–25	A	36
1989 Mar 31	B	9.5
1989 Apr 1 & 6	B	2.5, 24.5
1989 July 2	C	18
1989 Sept 14	C	1.5
1989 Nov 24	D	3.2
1989 Dec 26 & 31	D	2, 2
1991 May 13	D	0.4

Column 2 lists the configuration of the VLA and column 3 the total (source and calibrator) observation time in that configuration on that date.

Table 3. VLA observations for sources presented in this paper.

Source	τ_{obs}(min)				$\Delta\nu$(MHz)			
	A	B	C	D	A	B	C	D
3C197.1	56	79	15	–	50	50	50	–
3C223.1	114	88	11	10	25	25	50	50
3C227P	180	46	21	10	12	25	50	50
3C227F	86	43	23	11	50	50	50	50
3C382	–	78	25	21	–	25	50	50
3C403P	–	39	23	8	–	50	50	50
3C403F	56	37	25	9	50	50	50	50
3C424	74	56	22	10	50	50	50	50
3C433	186	76	30	–	25	25	50	–
3C452P	73	30	25	–	50	50	50	–
3C452F	–	30	25	–	–	50	50	–

Column 1 lists the source with the qualifier P or F denoting observations for which the primary beam was pointed at the preceding or following end of the source, respectively. Columns 2–5 give the approximate durations and columns 6–9 the bandwidths of observations in each VLA configuration.

3 DATA REDUCTION

3.1 Method

For the eight sources presented here, all data reduction was carried out using the NRAO Astronomical Image Processing System (AIPS) software. The data were calibrated in AIPS. Flux density calibration was based on 3C48 and 286 using the scale of Baars *et al.* (1977), adjusted as reported in the 1991 March VLA status report. Polarization angle calibration used the same calibrators. For each configuration, visibility data at the two frequencies were concatenated before any reduction and then treated as a single data set of effective frequency 8.350 GHz – with the enhanced u–v coverage achieved by the wide separation (230 MHz) of the two observation frequencies. From the work of Simard-Normandin, Kronberg & Button (1981), the integrated rotation measures (RM) for all of our eight sources are known to be such that *differential* Faraday rotation and depolarization (both between the two frequencies and across the band) are negligible (see Table 5).

The *general* self-calibration procedure (Cornwell & Fomalont 1989) was as follows. The first data available, the C-data, were self-calibrated to good convergence, usually through two phase self-calibrations, and used in the self-calibration of the D-data. B-data were phase self-calibrated usually twice using a CLEAN BCD-model (where we use BCD to denote the concatenated databases of B + C + D-configuration data). A-data were then phase self-calibrated once with an ABCD-CLEAN map; here convergence was often poor due to the low flux densities detected in A-configuration and the necessarily short duration of the solution time τ_{sol}. Finally, the concatenated ABCD-database was phase self-calibrated with an ABCD-data CLEAN model. A similar self-calibration procedure was adopted for sources with only BCD- or BC-data.

Once their individual self-calibrations were complete but before concatenating them, the data from each array were time-averaged for ease of computation. The averaging time τ_{ave} was chosen to be less than the critical smearing times, τ_{smear}. (See Table 4: δ_{max} is the angular displacement from the phase centre at which the smearing time τ_{smear} will produce a loss of 5 per cent in the vector-averaged amplitude of the recorded fringes.) A practical *lower* limit is set by the instrumental integration time, τ_{int}, and an *upper* limit was arbitrarily chosen as 120 s. In subsequent self-calibrations, visibility points in the concatenated databases have the (AIPS-) assigned weight of $\tau_{ave}/(10\ s)$.

Typical values of the critical self-calibration parameters used for A-, B-, C- and D-configuration data respectively were as follows: solution time-interval $\tau_{sol} \simeq 30, 120, 300$ and 30 s, minimum baseline $\simeq 100, 20, 10$ and 5 kλ, no maximum baseline specified. For D-configuration data, the high flux density and correspondingly high signal-to-noise ratio allows a self-calibration solution to be calculated from and applied to each visibility point *individually* (i.e. $\tau_{sol} = \tau_{int}$).

Table 4. Smearing times.

δ_{max} (arcsec)	τ_{smear} (s) A	B	C	D
20	80	250	800	2500
40	40	125	400	1250
60	26	80	260	800
80	20	60	200	600
100	16	48	160	130
120	13	40	130	400
140	11	35	110	350
160	10	30	100	300
180	9	26	90	260
200	8	24	80	240

Column 1 gives the angular displacement from the phase centre at which the averaging times given in columns 2–5 (for each VLA configuration) produce a loss of 5 per cent in amplitude when the recorded fringes are (vector-) time-averaged.

3.2 Mapping

The AIPS Maximum Entropy (MEM) deconvolution program VTESS (Cornwell 1989) was used to produce all the final total intensity maps – this was preferred to the more conventional CLEAN algorithm for reasons to do with mapping multiconfiguration (ABCD-) data. However, VTESS is notoriously bad (as are all MEM algorithms) at deconvolving sidelobes about bright, compact features such as cores, and tends to produce 'ringing' artefacts. This problem was overcome by applying the following hybrid technique: a shallow CLEAN was made of the brightest, most compact features and these components were subtracted in the u–v plane from the full database. The VTESS procedure was then applied to this database. The CLEAN components were then convolved with the chosen restoring beam and added back to the VTESS map. Alternatively, following a shallow CLEAN, VTESS was applied to the residual map after which the convolved CLEAN components were added back. Both methods are denoted by CM in Table 6.

An image created by VTESS is the maximum entropy model *convolved* with the specified Gaussian restoring beam and added back to the 'residual' map. This smoothing should overcome any scepticism of signel-to-noise dependent resolution which some have for MEM images. (The 'residual' map is that which remains once the best MEM model has been subtracted from the visibility data in the u–v plane, analogous to the residual map remaining when the best CLEAN model has been subtracted from the data.)

When imaging the Stokes parameters Q and U, the hybrid technique was not needed, since the cores do not have significant polarized flux. The Q and U images were deconvolved using UTESS (T. Cornwell, in preparation), a program available in AIPS which employs an algorithm based on MEM, though not constrained by positivity: here too the final model is convolved with a Gaussian beam and added back to the residual map.

When the size of the source and its u–v database allowed, the entire source was imaged in a single field, but for some of the largest sources, the exceptionally large u–v databases (up to 10^6 visibility points) made mapping of the entire source, at highest resolution, computationally prohibitive. Fortunately, at the highest resolution, most of the extended structure is resolved out and so produces very weak sidelobes. A subfield around the hotspot was therefore mapped and deconvolved (with the core subtracted out in the u–v plane when necessary) and the weak sidelobes of any excluded structure were ignored.

For three of the eight sources presented, the pointing centre was located at each end of the source and two independent databases collected (denoted P and F as described in Section 2 and shown in Table 3). When mapping the entire source at lower resolution (2.5 arcsec) the data were mapped and deconvolved for each end separately, the primary beam corrections applied and the maps finally combined using the 'mosaicing' capability of the AIPS task VTESS (Cornwell 1989).

The imaging method adopted for each source is summarized in Table 6.

4 RESULTS

For several sources, the theoretical noise level could not be achieved because of residual calibration errors (which become apparent with very high surface brightness components, for example 3C382 with a dynamic range of $\simeq 7500{:}1$) and residual sidelobes (for sources where only selected subfields were deconvolved), but multiple self-calibration and critical data editing allowed the theoretical noise level to be approached for most of the sources. For our observations, the new and most sensitive VLA receiver system at 8 GHz gave a limiting thermal noise in total intensity of

$$\sigma_I^{\rm thermal} \simeq 1075[(\tau_{\rm obs}/{\rm min})(\Delta\nu/{\rm MHz})]^{-1/2}\ \mu{\rm Jy\ beam}^{-1}$$

for on-source observations of duration $\tau_{\rm obs}$ with a bandwidth of $\Delta\nu$.

Typically, the noise level actually achieved is $\sigma_{\rm I} \simeq 40\ \mu$Jy beam^{-1}. The Stokes Q and U maps are nearly always thermal-noise limited with typical noise levels in the polarized flux of $\sigma_{\rm P} = \sigma_{\rm Q} = \sigma_{\rm U} \simeq 28\ \mu$Jy beam^{-1}.

Tables 5 and 6 summarize the properties of the final images. The image resolution (FWHM) is given in arcsec and in kpc. The noise levels are given for total intensity ($\sigma_{\rm I}$) and polarized intensity ($\sigma_{\rm P}$) maps. The dynamic range (DR) is the ratio of the peak in total intensity ($I_{\rm pk}$) to the noise ($\sigma_{\rm I}$).

We present total intensity and fractional polarization maps of our eight sources (Figs 1–26): in each case high-resolution images of the hotspot regions are supplemented by an image of the entire source, at a lower resolution for most.

The polarization vectors are of length proportional to the degree of polarization [$m = P/I$ where the polarized intensity $P = (Q^2 + U^2)^{1/2}$] and orientation equal to that of the

Table 5. Information for sources presented in this paper.

Source	scale (kpc arcsec^{-1})	D (kpc)	RM (rad m^{-2})	Jet lobe	Jet feature	Jet flux density (mJy)
3C197.1	3.15	56	-5±2	–	–	–
3C223.1	2.69	230	+3±4	Sf	N4	5±1
3C227	2.21	520	-7±2	–	–	–
3C382	1.55	290	123±?	Np	N2,3,5	84±1
3C403	1.57	170	-36±1	Nf	F7,8	23±1
3C403	"	"	"	Nf	F4,5	19±1
3C424	3.10	100	-55±4	Np	N1,2,3	61±1
3C424	"	"	"	Sf	S1,2	54±1
3C433	2.56	150	-73±1	Np	N1,2,3,4	49±1
3C452	2.10	590	-275±1	Nf	P4,5	30±8
3C452	"	"	"	Sp	F4,5	24±4

Column 3 lists the linear extent of the source, along its main axis. Column 4 lists the rotation measures of Simard-Normandin, Kronbergy & Button (1981). Column 5 lists the lobe in which a jet is detected, where N denotes north, S south, p preceding and f following. Column 6 lists the features labelled in Figs 1–26 which have been interpreted as components of jets, and column 7 lists the total radio flux at 8 GHz from these features (no correction has been made here for background lobe emission).

Table 6. Images for sources presented in this paper.

source	Fig No.	region	method	*FWHM* ($''$)	*FWHM* (kpc)	σ_I (μJy)	σ_P (μJy)	*DR* (I_{pk}/σ_I)
3C197.1	1a/b	whole	CM/M	0.25	0.8	19	17	290
	2a/b	HS(Nf)	”	”	”	”	”	”
	3a/b	HS(Sp)	”	”	”	”	”	”
3C223.1	4a/b	whole	CM/M	2.50	6.7	55	36	800
	5a/b	HS(Nf)	CM/C	0.25	0.7	18	23	330
	6a/b	HS(Sp)	”	”	”	”	”	”
3C227	7a/b	whole	M/M	2.50	5.5	130	49	500
	8a/b	HS(Sp)	M/C	0.25	0.6	29	33	10700
	9a/b	HS(Sf)	”	”	”	”	”	”
3C382	10a/b	whole	CM/M	0.75	1.2	40	28	7500
	11a/b	HS(Nf)	”	”	”	”	”	”
	12a/b	HS(Sp)	”	”	”	”	”	”
3C403	13a/b	whole	CM/CM	2.50	3.9	50	40	1200
	14a/b	HS(Np)	M/M	0.75	1.2	38	25	710
	15a/b	HS(Sf)	CM/CM	0.25	0.4	38	19	340
3C424	16a/b	whole	CM/M	0.75	2.3	28	28	780
	17a/b	HS(Np)	CM/C	0.25	0.8	19	25	410
	18a/b	HS(Sf)	”	”	”	”	”	”
3C433	19a	whole	M/M	0.25	0.6	16	15	100
	20b	N jet	”	”	”	”	”	”
	21b	S lobe	”	”	”	”	”	”
	22b	S lobe	”	”	”	”	”	”
	23b	core	”	”	”	”	”	”
3C452	24a/b	whole	CM/CM	2.50	5.3	75	50	3100
	25a/b	HS(Sp)	”	0.25	0.5	28	17	90
	26a/b	HS(Nf)	”	0.75	1.6	53	28	60

In column 2, the suffix a denotes images of total intensity and b of fractional polarization. Column 3 lists the region covered by the map – a map of the entire source is denoted by 'whole' and detailed subimages around each hotspot alone by HS (in the lobe qualified in parentheses). Column 4 lists the deconvolution algorithm relevant to the a and b maps listed in column 2; C denotes CLEAN, M a maximum entropy algorithm (VTESS) and CM the hybrid CLEAN–VTESS (outlined in Section 3.2). Column 5 gives the FWHM of the restoring beam and column 6 its linear size. Columns 7 and 8 list the noise levels on the total intensity and polarized intensity maps, respectively. Column 9 gives the dynamic range.

observed E-vector ($\tan\phi = Q/U$): these are plotted only where $I > 4\sigma_I$ and are superimposed on total intensity contours that are multiples of the estimated noise level. No attempt has been made to correct for Faraday rotation; the small corrections ($\Delta\phi_8$) predicted for observations at 8 GHz (3.6 cm) using the integrated rotation measures, taken from the literature, are given for each map and should be added in a *clockwise* sense.

On the grey-scale images and contour maps the position of the associated galaxy is indicated by a cross; a linear scale-line labelled in kpc is, for most, in the top right-hand corner; the FWHM of the restoring beam is shown as a hatched

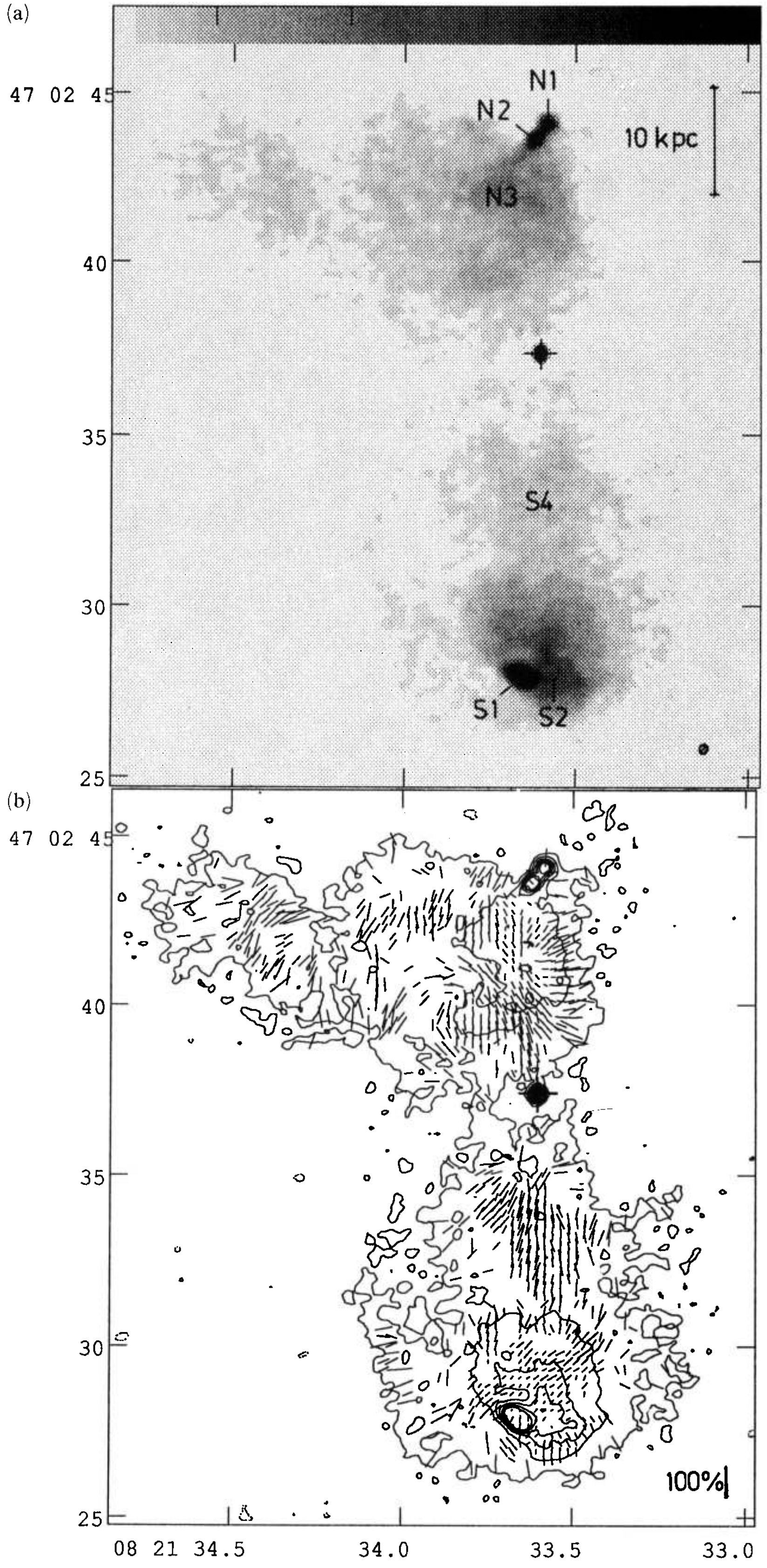

Figure 1. 3C197.1 at 0.25-arcsec resolution. (a) Grey-scales are shown for 0.05 mJy beam^{-1} (white) to 1 mJy beam^{-1} (black). (b) Contours are shown at (−3, 3, 10, 20, 30, 40, 50, 100, 150, 200, 300) × 20 μJy beam^{-1} and $\Delta\phi_8 \simeq 0°$.

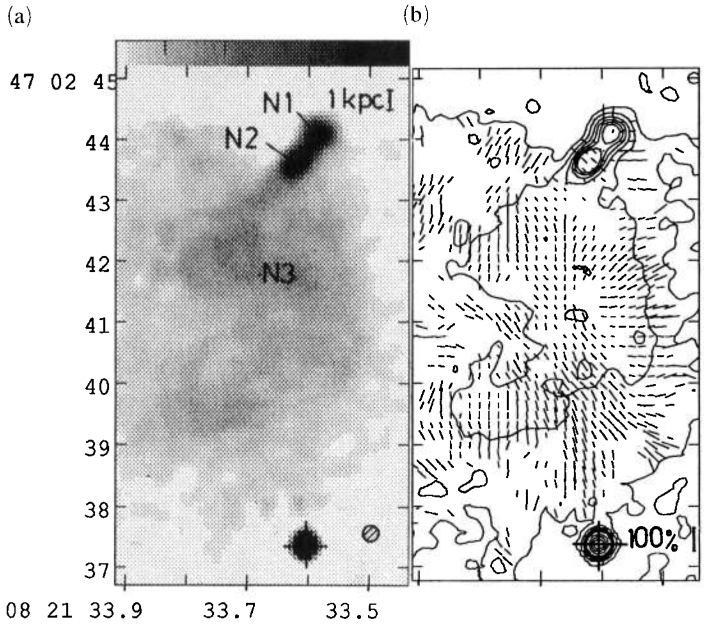

Figure 2. Hotspot in Nf lobe of 3C197.1 at 0.25-arcsec resolution. Captions as for Fig. 1.

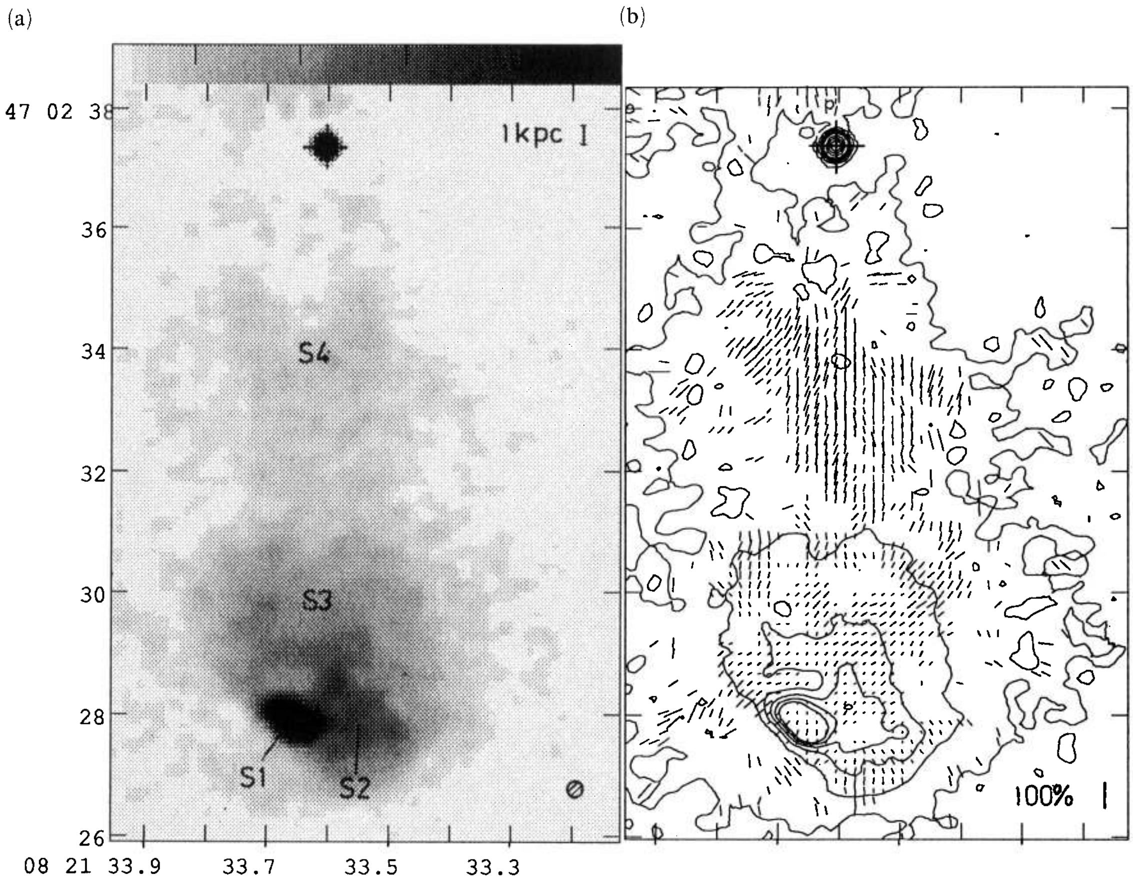

Figure 3. Hotspot in Sp lobe of 3C197.1 at 0.25-arcsec resolution. Captions as for Fig. 1.

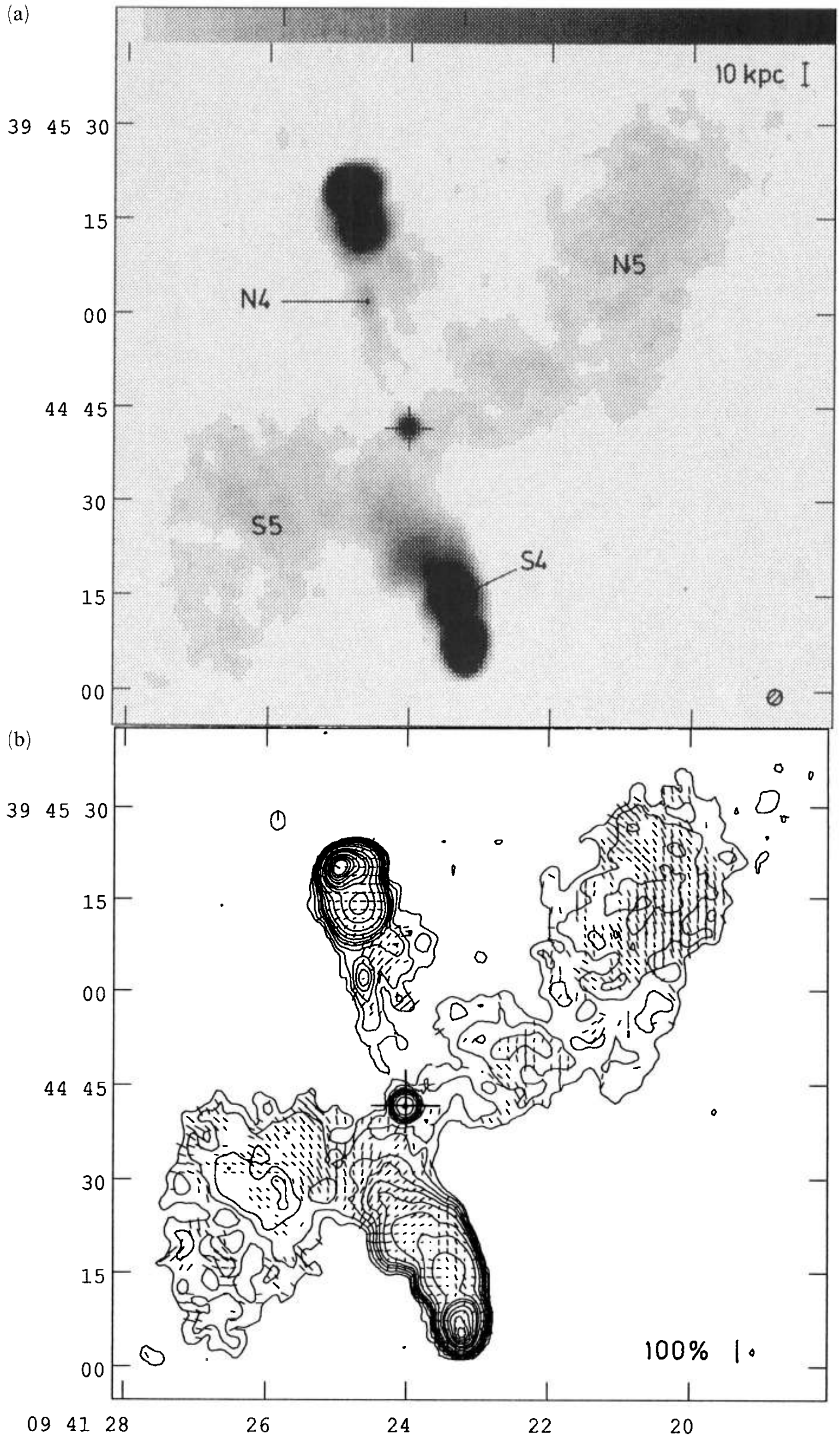

Figure 4. 3C223.1 at 2.5-arcsec resolution. (a) Grey-scales are shown for 0.1 mJy beam^{-1} (white) to 4 mJy beam^{-1} (black). (b) Contours are shown at (− 4, 4, 6, 9, 12, 15, 20, 30, 50, 100, 150, 200, 300, 400, 500, 600) × 55 μJy beam^{-1} and $\Delta\phi_8 \simeq 0°$.

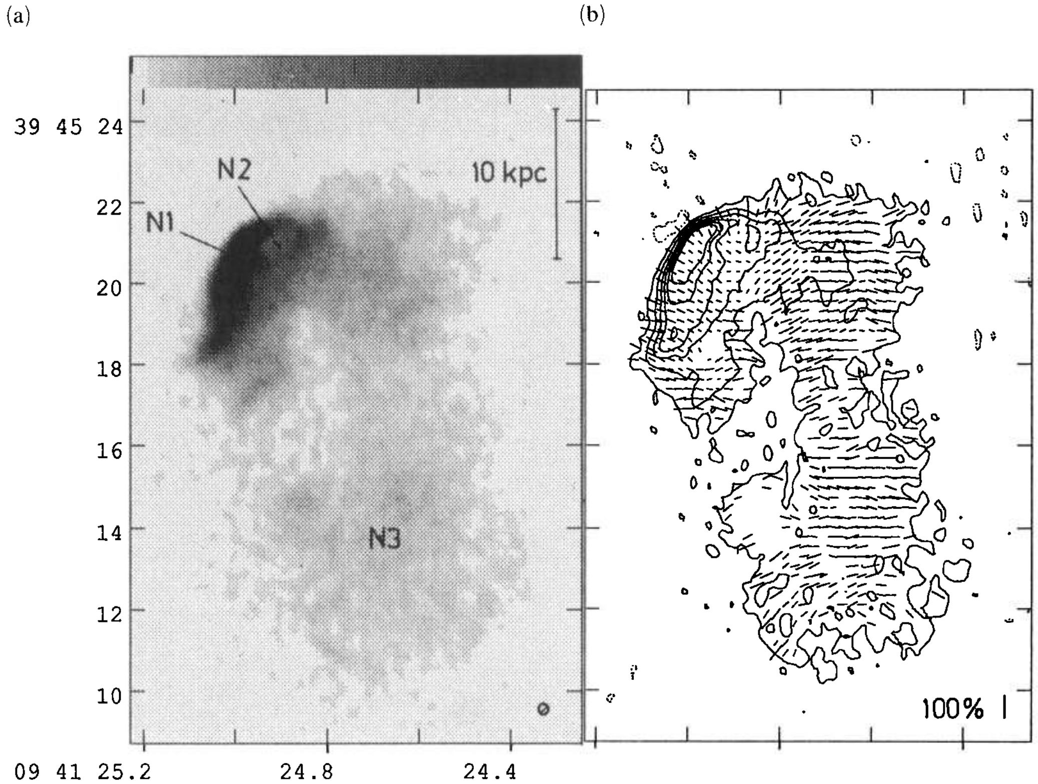

Figure 5. Hotspot in Nf lobe of 3C223.1 at 0.25-arcsec resolution. (a) Grey-scales are shown for 0 mJy beam^{-1} (white) to 1 mJy beam^{-1} (black). (b) Contours are shown at $(-3, 3, 10, 20, 30, 40, 50, 100, 150, 200, 300) \times 20$ μJy beam^{-1} and $\Delta\phi_8 \simeq 0°$.

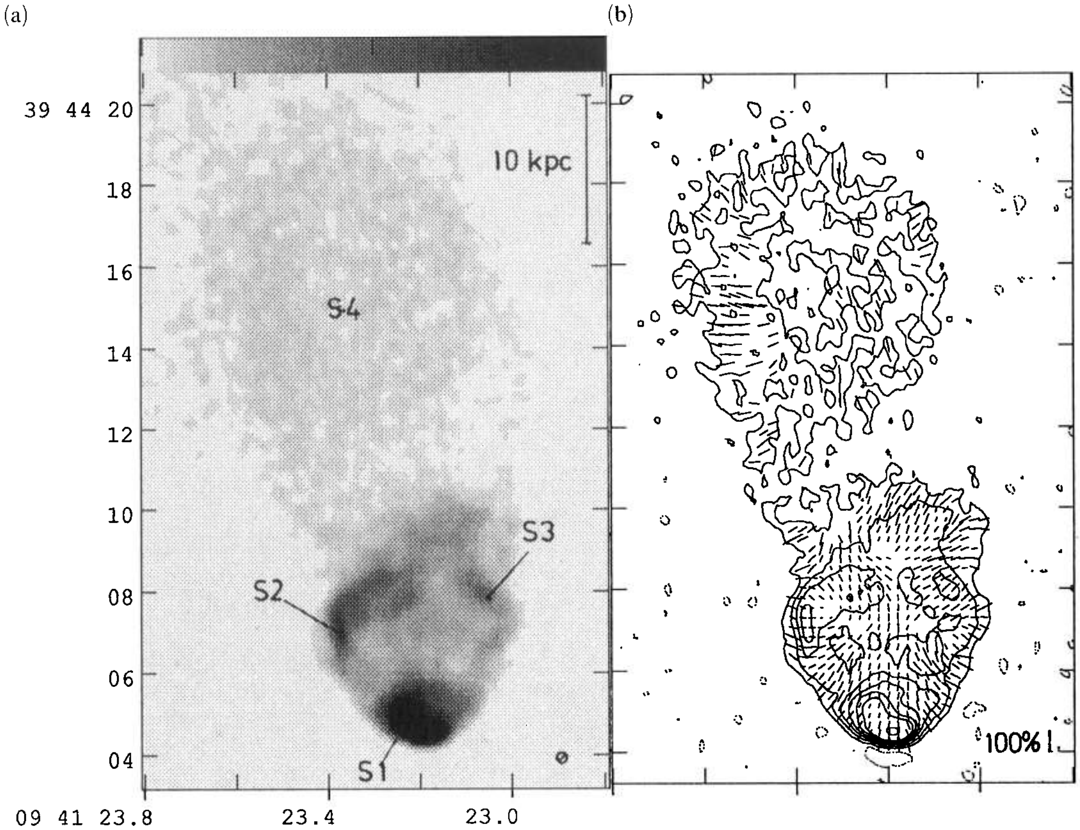

Figure 6. Hotspot in Sp lobe of 3C223.1 at 0.25-arcsec resolution. Captions as for Fig. 5.

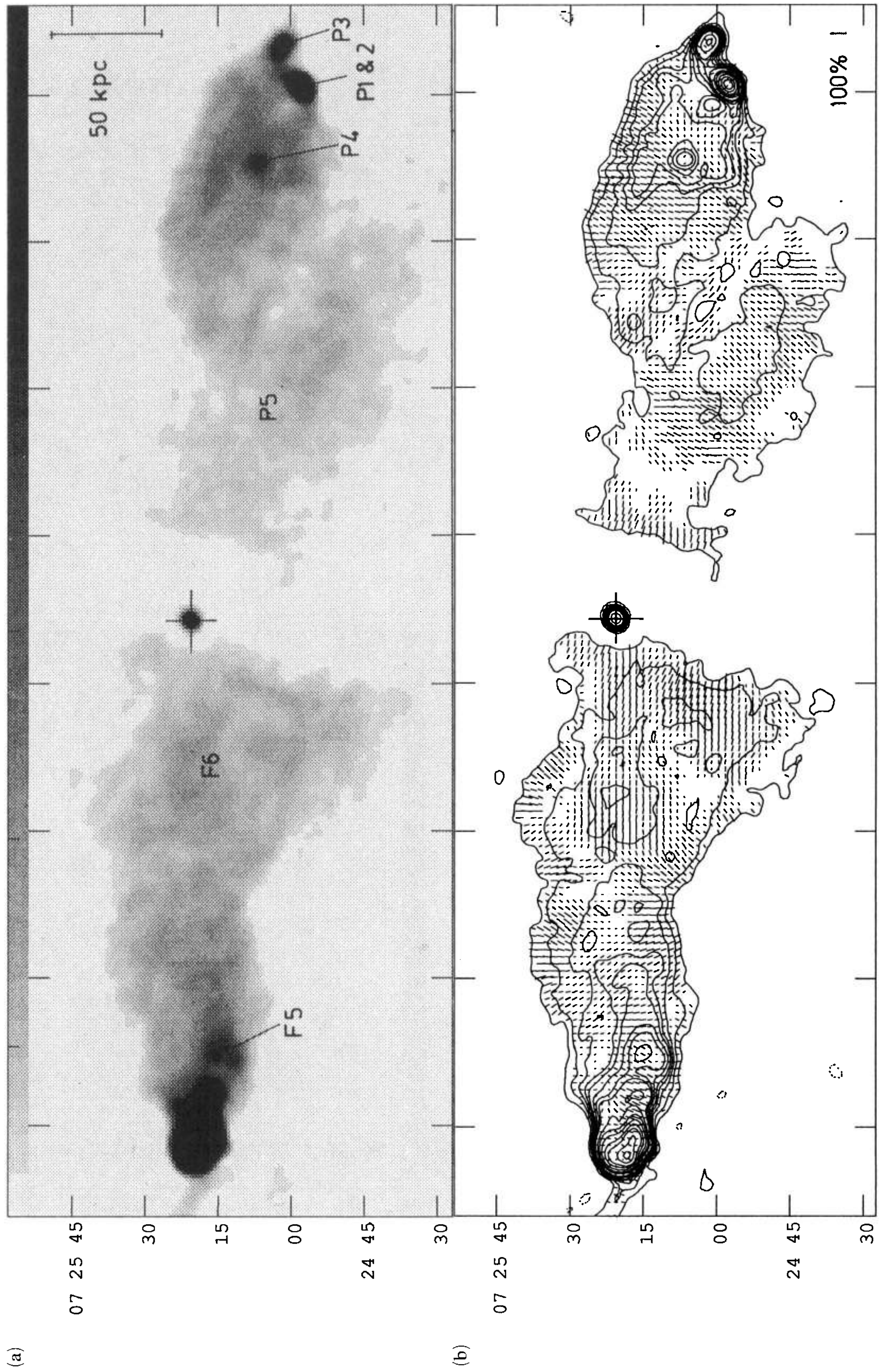

Figure 7. 3C227 at 2.5-arcsec resolution. (a) Grey-scales are shown for 0.2 mJy beam^{-1} (white) to 6 mJy beam^{-1} (black). (b) Contours are shown at (−3, 3, 6, 9, 12, 15, 20, 25, 30, 50, 70, 100, 150, 200, 300, 400, 500) × 150 μJy beam^{-1} and $\Delta\phi_8 = 0°$.

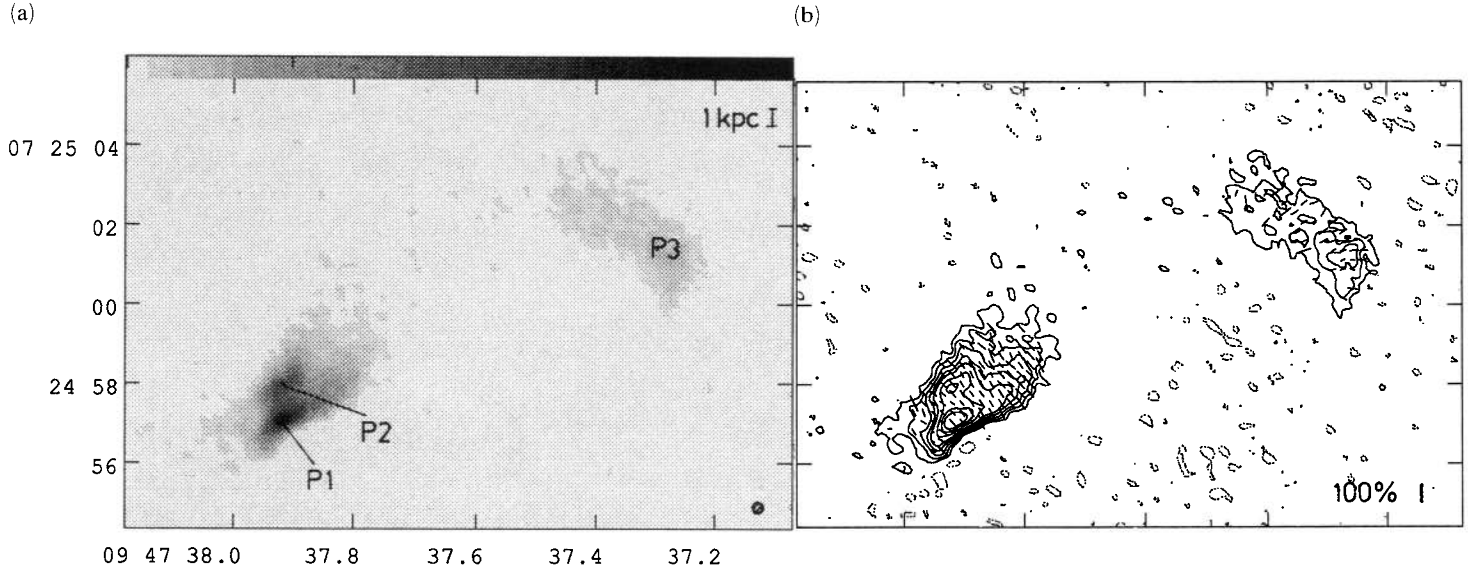

Figure 8. Hotspot at end of Sp lobe of 3C227 at 0.25-arcsec resolution. (a) Grey-scales are shown for 0 mJy beam^{-1} (white) to 2 mJy beam^{-1} (black). (b) Contours are shown at $(-3, 3, 6, 10, 15, 20, 30, 40, 50) \times 25$ μJy beam^{-1} and $\Delta\phi_8 \simeq 0°$.

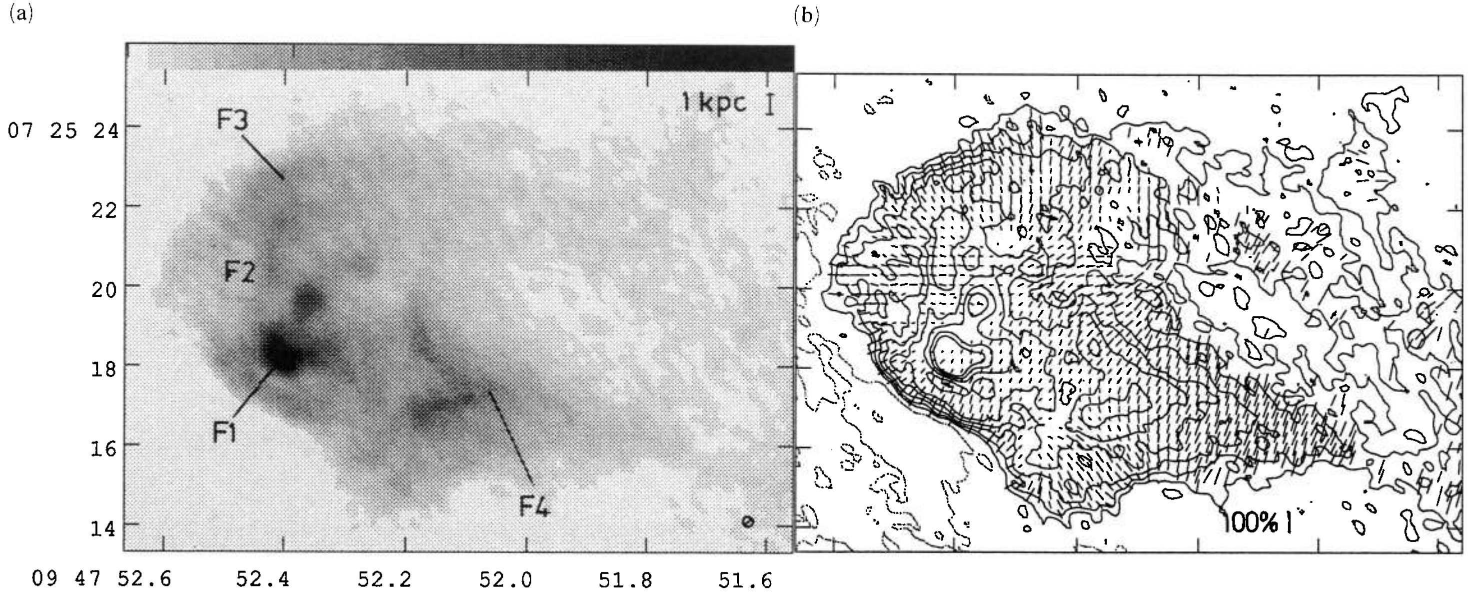

Figure 9. Hotspot at end of Sf lobe of 3C227 at 0.25-arcsec resolution. Captions as for Fig. 8.

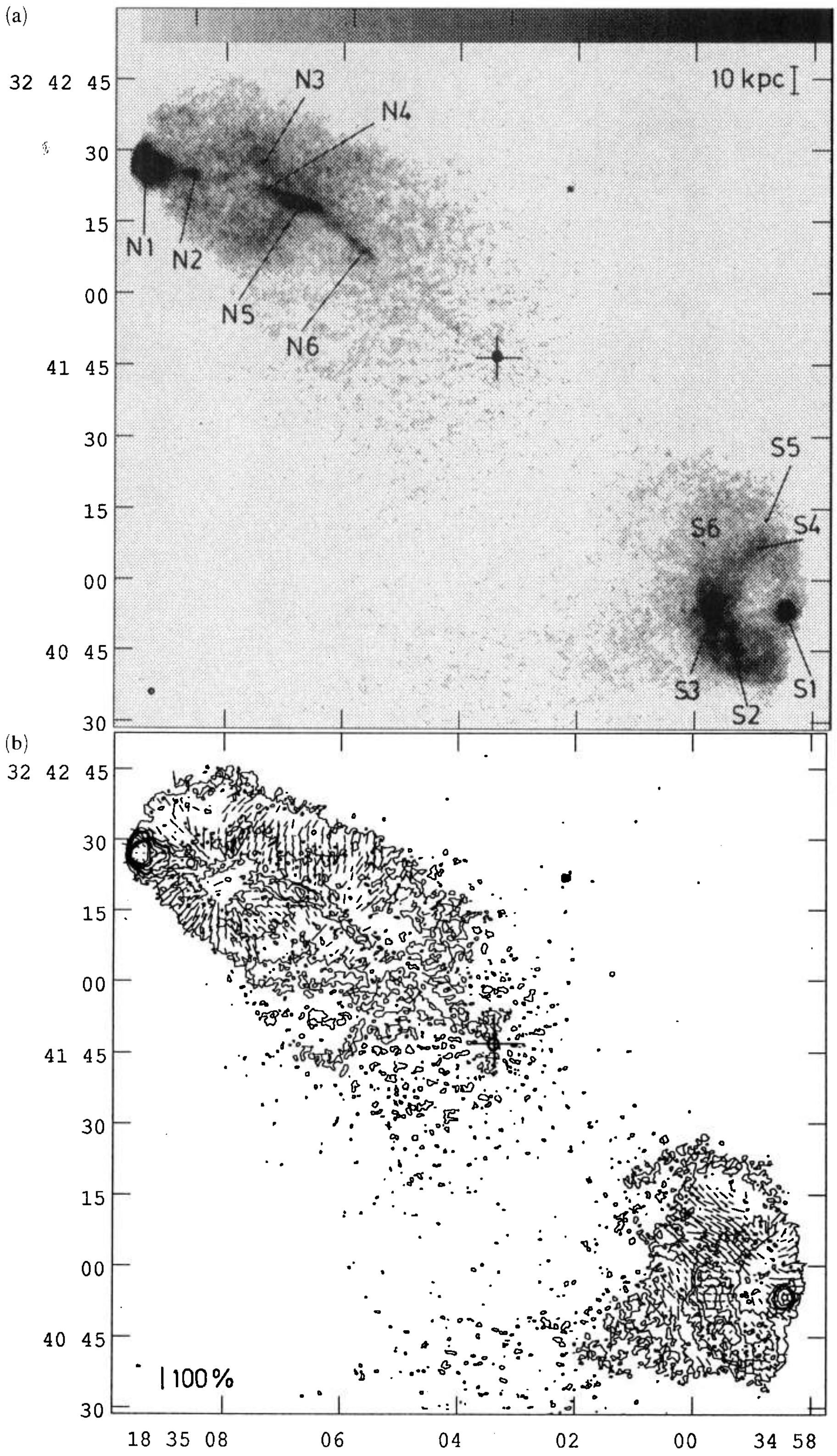

Figure 10. 3C382 at 0.75-arcsec resolution. (a) Grey-scales are shown for 0.05 mJy beam^{-1} (white) to 1 mJy beam^{-1} (black). (b) Contours are shown at $(-4, 4, 10, 15, 20, 30, 50, 70, 100) \times 20\ \mu$Jy beam^{-1} and $\Delta\phi_8 \simeq 9°$.

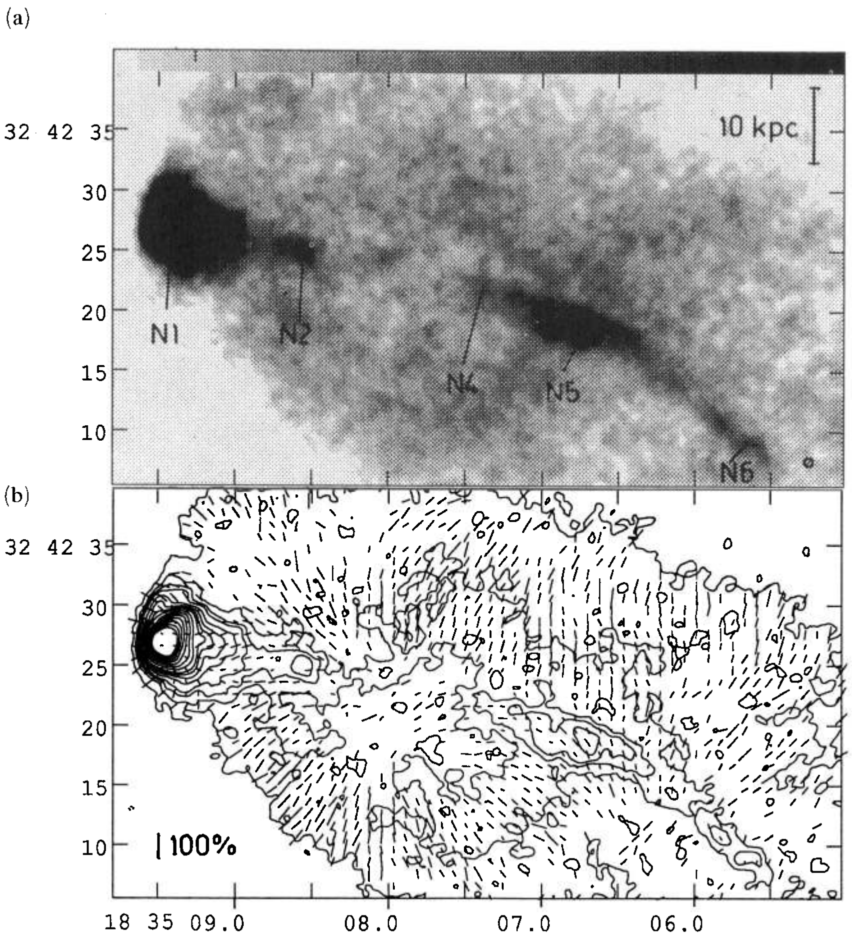

Figure 11. Hotspot in Nf lobe of 3C382 at 0.75-arcsec resolution. (a) Grey-scales are shown for 0.05 mJy beam^{-1} (white) to 0.5 mJy beam^{-1} (black). (b) Contours are shown at (− 4, 4, 10, 15, 20, 30, 40, 50, 60, 80, 100, 120, 140, 160, 180, 200) × 20 μJy beam^{-1} and $\Delta\phi_8 \simeq 9°$.

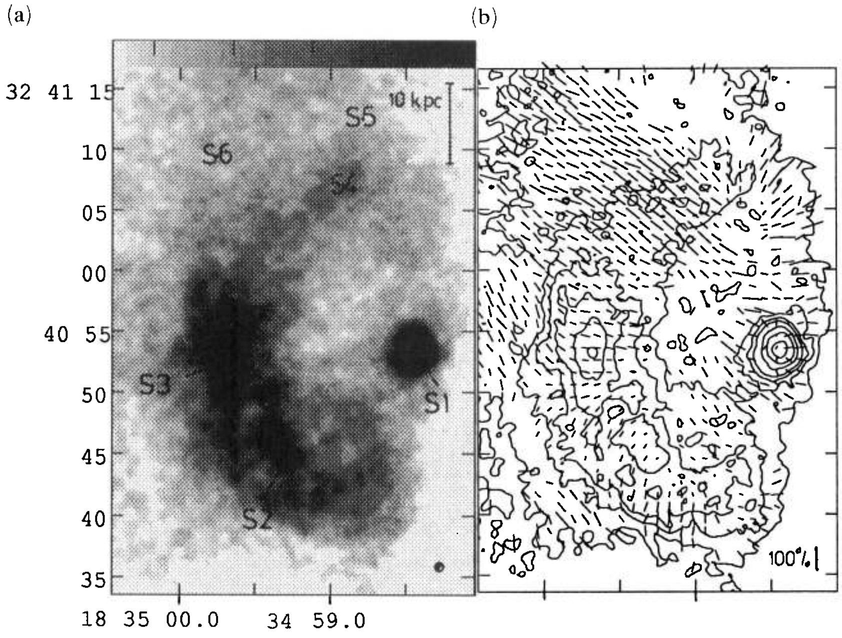

Figure 12. Hotspot in Sp lobe of 3C382 at 0.75-arcsec resolution. Captions as for Fig. 11.

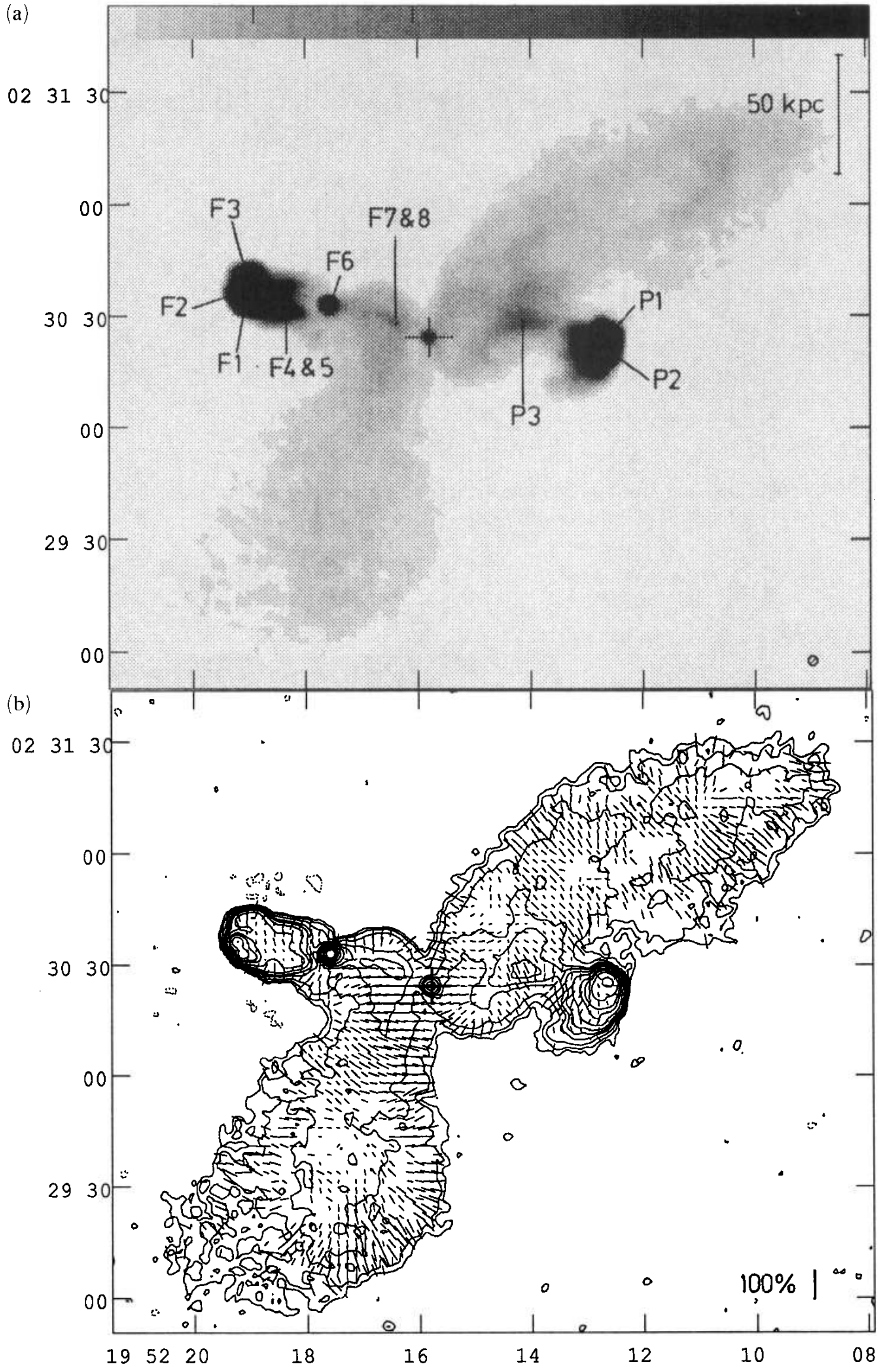

Figure 13. 3C403 at 2.5-arcsec resolution. (a) Grey-scales are shown for 0.1 mJy beam^{-1} (white) to 5 mJy beam^{-1} (black). (b) Contours are shown at $(-3, 3, 5, 10, 20, 30, 50, 100, 200, 300, 500, 1000) \times 50$ μJy beam^{-1} and $\Delta\phi_8 \simeq -3°$.

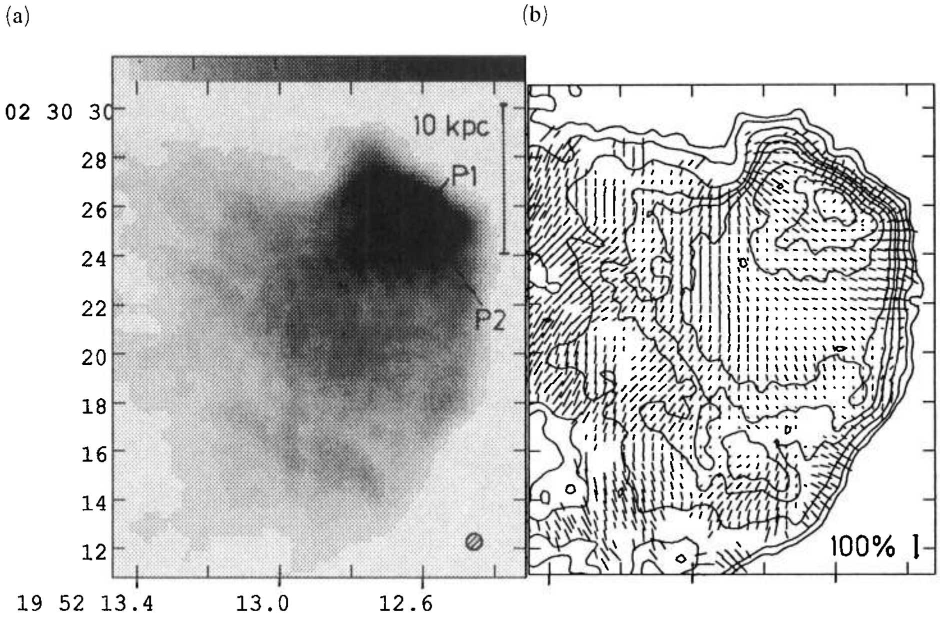

Figure 14. Hotspot in Sp lobe of 3C403 at 0.75-arcsec resolution. (a) Grey-scales are shown for 0.05 mJy beam^{-1} (white) to 0.5 mJy beam^{-1} (black). (b) Contours are shown at (−3, 3, 5, 10, 20, 30, 50, 100, 150, 200, 300, 400)×35 μJy beam^{-1} and $\Delta\phi_8 \simeq -3°$.

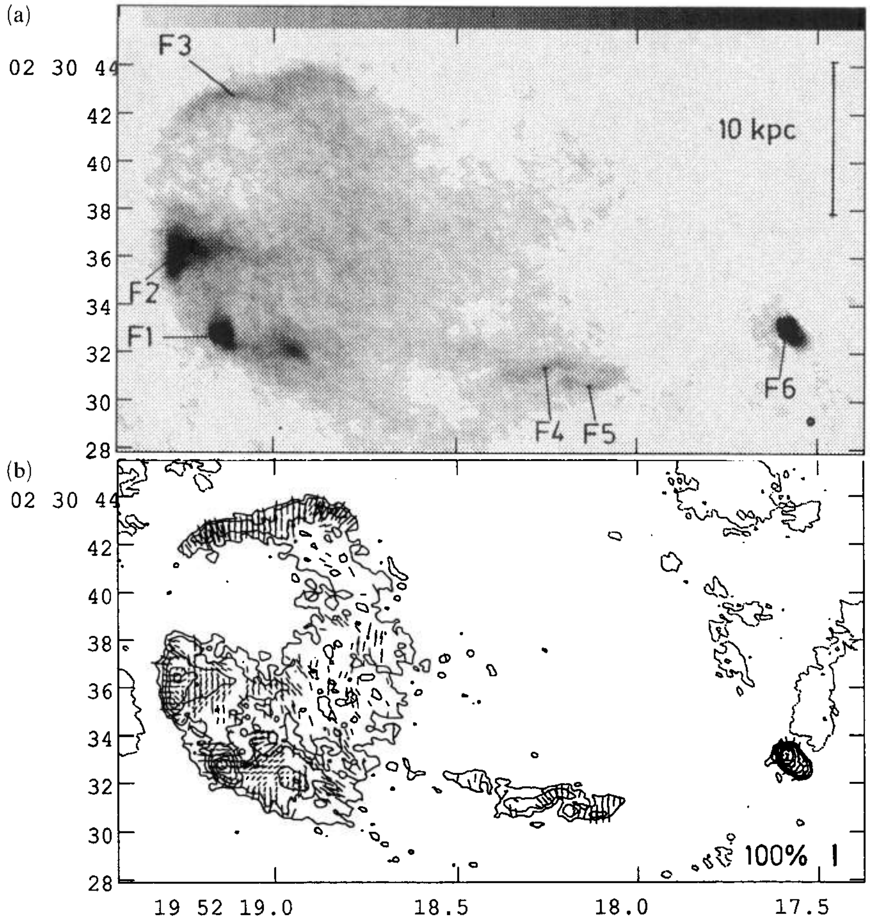

Figure 15. Hotspot in Nf lobe of 3C403 at 0.25-arcsec resolution. (a) Grey-scales are shown for 0 mJy beam^{-1} (white) to 1 mJy beam^{-1} (black). (b) Contours are shown at (−3, 3, 5, 10, 20, 50, 100, 300)×40 μJy beam^{-1} and $\Delta\phi_8 \simeq -4°$.

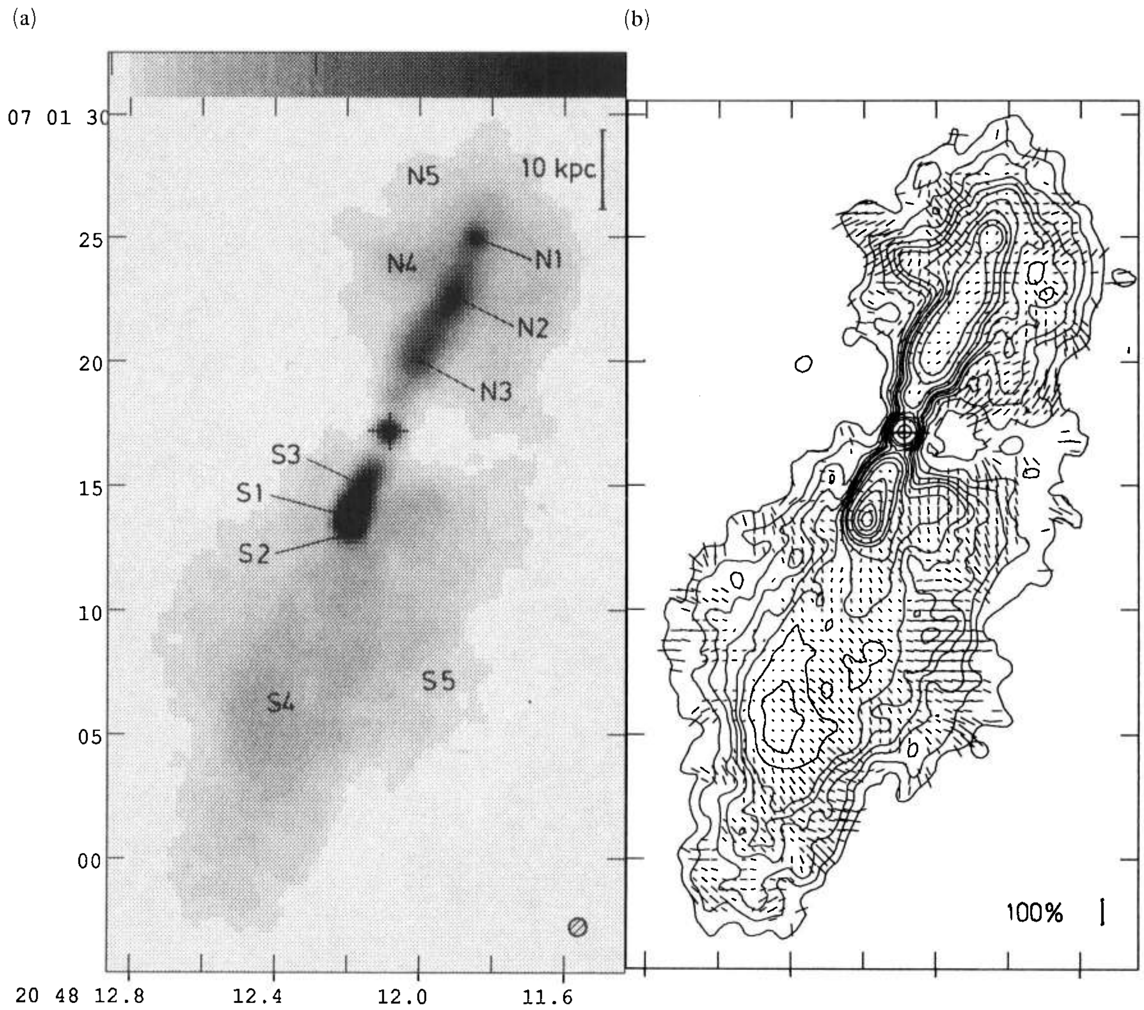

Figure 16. 3C424 at 0.75-arcsec resolution. (a) Grey-scales are shown for 0 mJy beam^{-1} (white) to 5 mJy beam^{-1} (black). (b) Contours are shown at (−5, 5, 10, 1, 20, 25, 30, 40, 50, 70, 100, 200, 300, 500, 700) × 25 μJy beam^{-1} and $\Delta\phi_s \simeq -4°$.

circle and a demonstration polarization vector (representing a specified fractional polarization) is in the bottom right-hand corner, unless shown otherwise. The coordinates are J2000.

5 COMMENTS ON INDIVIDUAL SOURCES

3C197.1 (Figs 1–3) – the relatively small linear size of this source ($D \sim 56$ kpc) suggests that it lies largely within the associated galaxy.

The Sp and Nf lobes show hotspots of similar surface brightness, size and shape. No jets are detected, although an unusual S-shaped bridge (N3) twists northwards to terminate in a remarkably compact, sub-kpc double hotspot. The fractional polarization is high through feature N2 (~35 per cent) and in a thin, unresolved (<0.8 kpc) cap feature N1 (~20 per cent): the *E*-field swings through 90° between N2 (where it is perpendicular to the axis N2–N1) and N1 (where it is radial). The hotspot S1 in the Sp lobe also shows a sharp boundary with high fractional polarization (~30 per cent): the sharp boundary of S1 is recessed from the edge of the lobe.

3C223.1 (Figs 4–6) – at lower resolution, this has a classic X-shape; extended wings are detected (with type 2 distortion, Leahy & Williams 1984) stretching 230 kpc north-west and 160 kpc south-east with fractional polarization reaching ~30 per cent. Furthermore, a weak jet N4 (~825 μJy beam^{-1}) is detected mid-way between the core and the western side of the hotspot in the Nf lobe: at higher resolution this feature is resolved out and is undetected.

The hotspot in the Nf lobe shows a very sharply defined boundary N1 which is highly polarized (~40 per cent): a region N2 of low, polarized intensity and fractional polarization sits in the most northern part of this hotspot. The Sp lobe shows a compact hotspot S1 of high fractional polarization (~50 per cent) in a bright, flat cap of emission (including features S1, S2 and S3): north of this is a peculiar ring structure, S4, of low surface brightness (~250 μJy beam^{-1}).

3C227 (Figs 7–9) – no obvious jet is detected in either lobe, though the following lobe has intermittent aligned structures reminiscent of a weak jet, through F5 and on to F4. The source axis is bent about the core, by ~14° to the south. The lobes cut off abruptly near the core, at straight boundaries.

1992MNRAS.256..186B

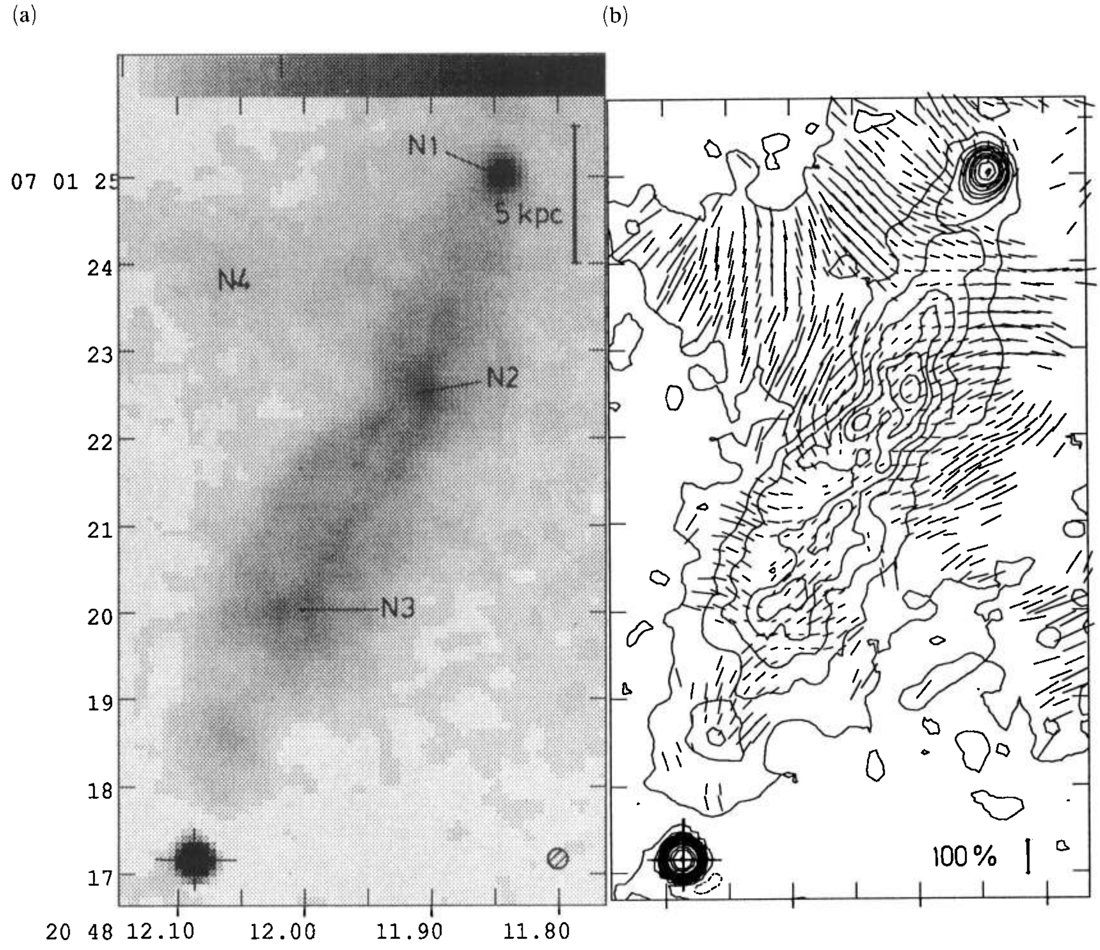

Figure 17. Detail in Np lobe of 3C424 at 0.25-arcsec resolution. (a) Grey-scales are shown for 0 mJy beam^{-1} (white) to 1.5 mJy beam^{-1} (black). (b) Contours are shown at $(-3, 3, 10, 15, 20, 25, 30, 40, 50, 60, 80, 100, 150, 200) \times 20$ μJy beam^{-1} and $\Delta\phi_8 \simeq -4°$.

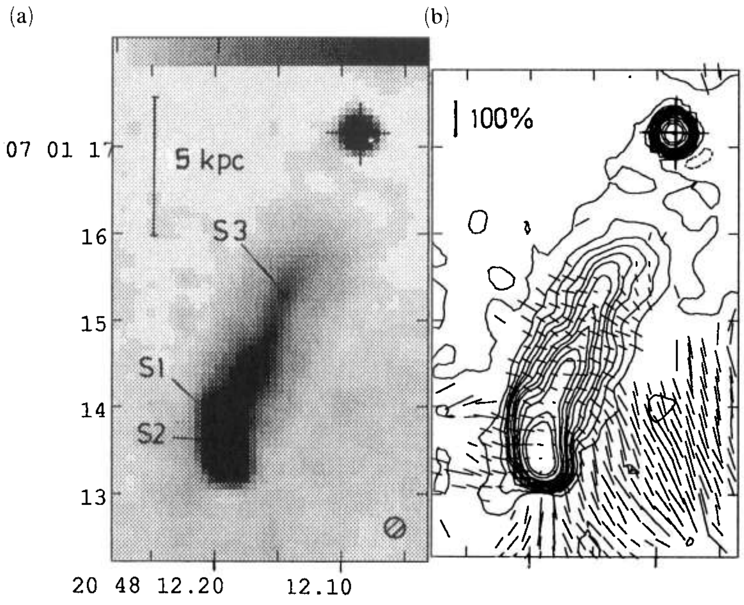

Figure 18. Detail in Sf lobe of 3C424 at 0.25-arcsec resolution. Captions as for Fig. 17.

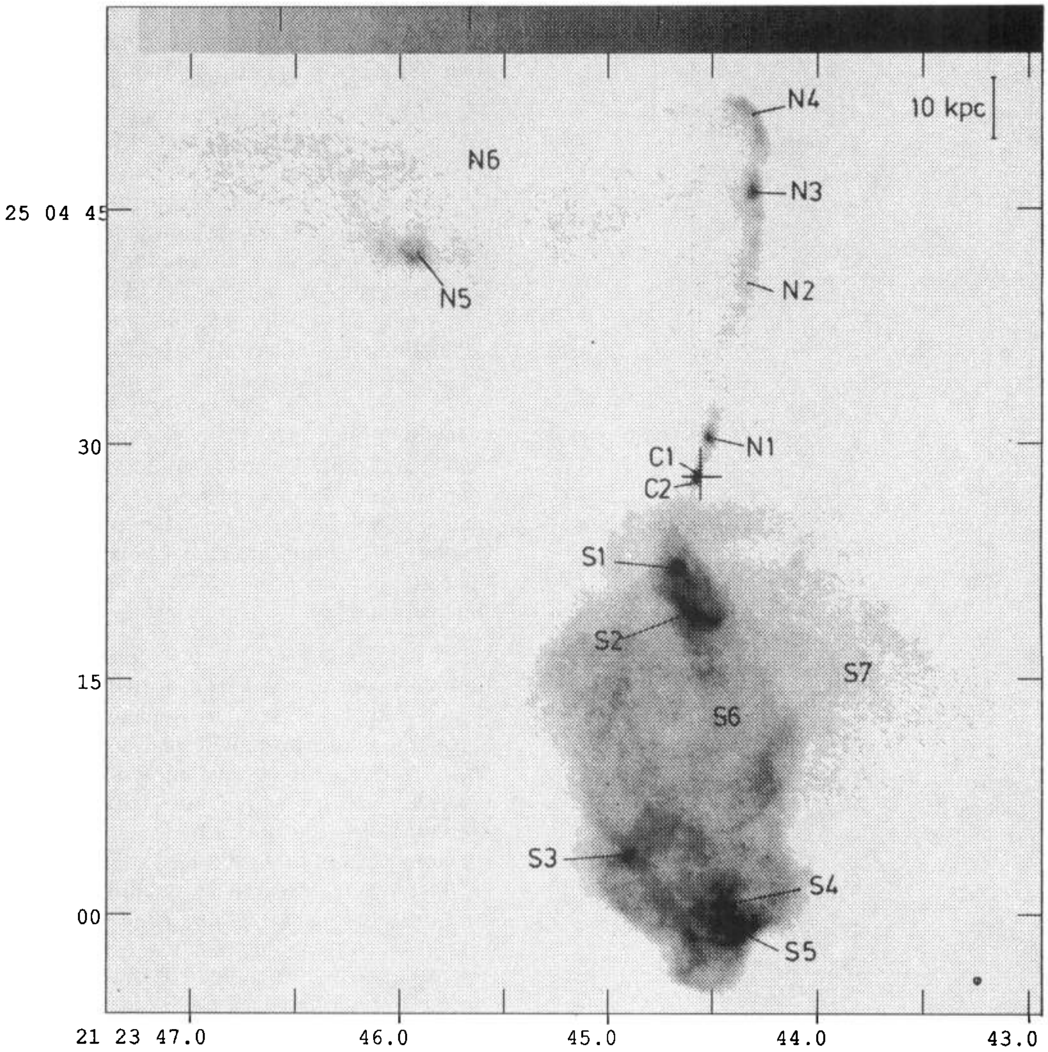

Figure 19. (a) 3C433 at 0.25-arcsec resolution. Grey-scales are shown for 0.02 mJy beam^{-1} (white) to 1 mJy beam^{-1} (black).

The Sp lobe shows two hotspot features, P1 and 2 and P3. The former shows remarkably small-scale (sub-kpc) structure, separating into P1 and P2: here fractional polarization is large (~ 40 per cent) and the *E*-vectors highly ordered.

The Sf lobe has a complex structure of filaments with ridge F4 of high fractional polarization (~ 50 per cent). Note also a curious cusp F2 which dents the end of this lobe.

3C382 (Figs 10–12) – no jet is observed in the southern lobe of 3C382, although a trail of *low* fractional polarization (⩽ 5 per cent) is detected, very reminiscent of a jet and its polarization properties: this feature enters the hotspot S1 from the north, after undergoing an abrupt deviation of ~ 45° at S5 from an apparent path from the core. This is far less apparent in total intensity. A ring feature of polarized emission links S1, S2, S3 and S4.

In the northern lobe, a diffuse (~ 5 kpc wide) and knotty jet is detected for the first time: this undergoes a deviation of ~ 25° through knot N5 and terminates in a compact and sharply defined hotspot, N1. Between N5 and N2, the jet passes across a ring of polarized emission with high fractional polarization (~ 50 per cent) which is not as apparent in total intensity; this is similar to that in the southern lobe. The terminating edge of hotspot N1 is well defined and shows complex layered structure in polarization (with fractional polarization reaching ~ 40 per cent).

3C403 (Figs 13–15) – this bizarre source shows many dramatic features.

At low resolution, 3C403 has a remarkable X-shape – wings stretch 130 kpc north-west and 100 kpc south-east: within these are regions of high fractional polarization common to such areas of low surface brightness.

The Sp lobe is tipped by an unusual hotspot P2 of uniform surface brightness, with no apparent substructure and an angular and abrupt boundary, labelled P1.

In the Nf lobe a weak jet (F7 and 8) is detected for the first time between the core and the exceptionally bright (13 mJy) knot F6. The knot F6 is partially resolved and extended to the south-west; it also shows high fractional polarization with *E*-vectors swinging from perpendicular to its axis (on entering from the south-west) to radial (at the north-eastern end).

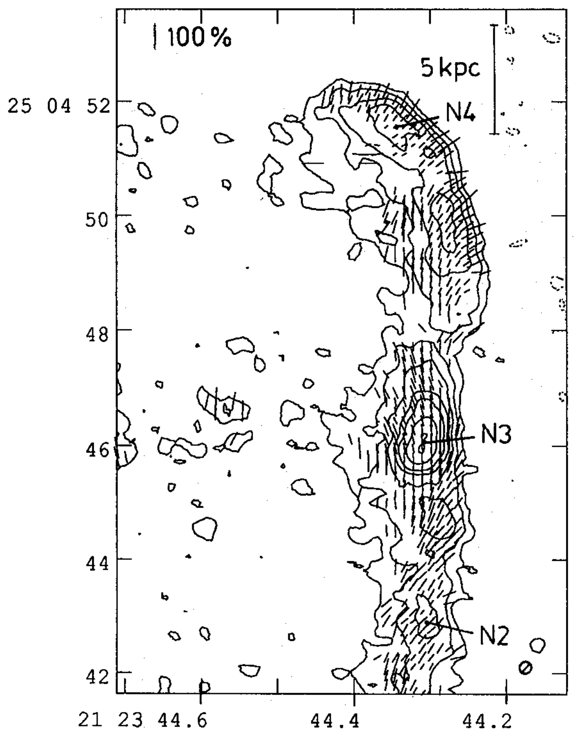

Figure 20. (b) Detail of features N2, N3 and N4 in N jet of 3C433 at 0.25-arcsec resolution. Contours are shown at (− 3, 3, 6, 10, 15, 20, 30, 40, 50, 60, 80, 100) × 15 μJy beam^{-1} and $\Delta\phi_8 \simeq -4°$.

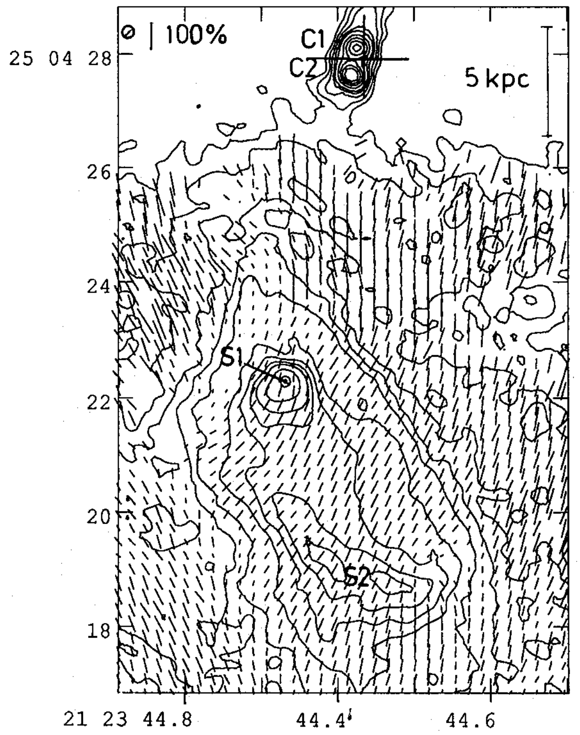

Figure 21. (b) Detail of features S1 and S2 in S lobe of 3C433. Captions as for Fig. 20(b).

Further east, the twisted features F4 and 5 appear to form another jet (but with no visible connection to F6) and terminate in the compact hotspot structures F1 and F2.

3C424 (Figs 16–18) – this small and extraordinary source (of projected linear diameter 100 kpc) shows none of the classic FRII structure.

Through the northern lobe twists a filamentary bridge N3 – reminiscent of a jet but unusually diffuse and apparently *converging* away from the core through N2, towards the very compact, sub-kpc hotspot, N1. The northern lobe is relatively faint and notably smooth in total intensity and of constant fractional polarization (~ 30 per cent): the *E*-vector orientation is swirling and complex.

In the more extended southern lobe a stunted jet S3 terminates 10 kpc from the core and has unresolved width of less than 1 kpc: *E*-vectors are highly ordered, running perpendicular to the axis but swinging sharply through 90° at the end. The south-eastern boundary of S1 shows an interesting feature, S2, of high fractional polarization (~ 40 per cent). The southern lobe of 3C424 is also quite uniform in total intensity and fractional polarization (~ 30 per cent).

3C433 (Figs 19–23) – this source has an unusually high luminosity for one with its distorted structure and small projected size (~ 150 kpc): it is unlike any classic FRII. These properties have prompted analysis of its gaseous environment which indicates the presence of considerable cold, turbulent gas, possibly associated with the merging of its central galaxy and a nearby (~ 10 arcsec north-east) companion (e.g., van Breugel *et al.* 1983; Yates & Longair 1989).

The images reveal much detail not previously seen. The central core (Figs 19, 21 and 23) is for the first time resolved into *two* compact components C1 and C2 separated by only ~ 1 kpc; no significant polarized flux is detected in either and the accuracy with which the position of the optical galaxy is known has not allowed identification of the 'true' core, if indeed there is only one. 2-cm observations with the VLA should resolve this problem.

Northwards, a knotty jet is traced through the bright knot N1, where fractional polarization reaches ~ 30 per cent and the *E*-vectors are orientated perpendicular to the jet axis, and on to features N2, N3 and N4. Both N3 and N4 show highly ordered *E*-vectors and high fractional polarization (~ 40 per cent). N5 too shows large fractional polarization (~ 40 per cent) and is not obviously connected to either N3 or N4. N5 could be the remnant dumping ground of material from a previous jet orientation (van Breugel *et al.* 1983).

The southern lobe cannot be adequately presented in a grey-scale plot: the detail in total intensity, polarized intensity and fractional polarization is a complex tangle of fine, sinewy structures. No jet is detected. A brighter ridge runs down the eastern side of the lobe from S1, and bifurcates at S3, one half leading through S4 to S5. The *E*-vectors show no global ordering but swirl smoothly throughout the southern lobe.

3C452 (Figs 24–26) – this large source (of projected linear size ~ 590 kpc) shows classic FRII morphology with noteworthy symmetry, even down to detail in the hotspots. A jet, P5 and 4, is clearly detected, with surface brightness ~ 1.2 mJy beam^{-1}, stretching westwards from a distance of 20 kpc from the core; it becomes lost in the lobe but when extrapolated further out appears to be in good alignment with the hotspot feature P2 and not with the brightest and most com-

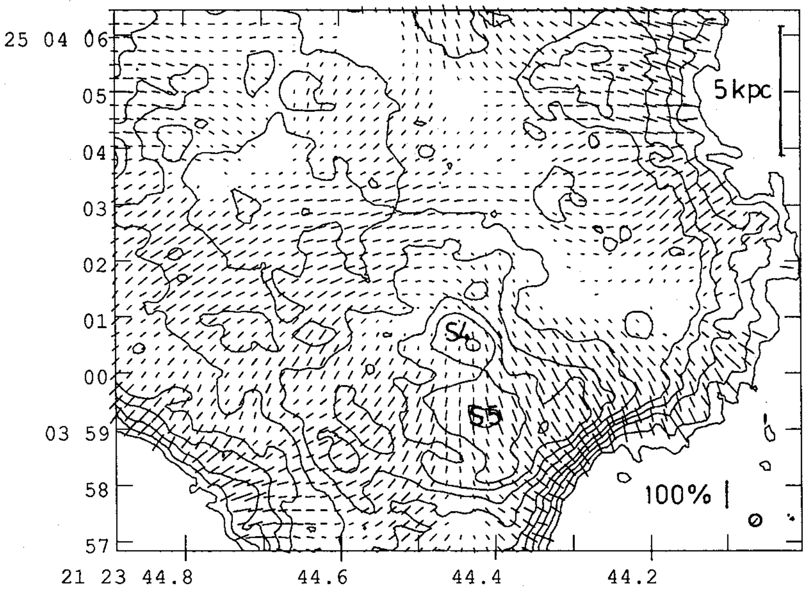

Figure 22. (b) Detail of features S4 and S5 in S lobe of 3C433. Captions as for Fig. 20(b).

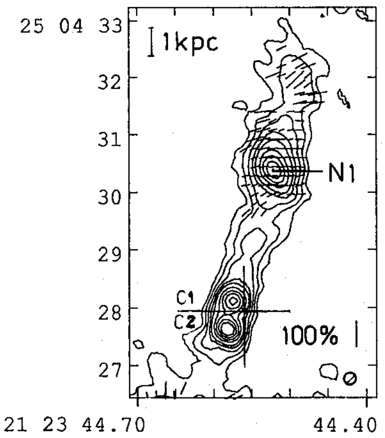

Figure 23. (b) Detail of double core C1 and C2 and feature N1. Captions as for Fig. 20(b).

pact hotspot P1. A counter-jet F5 and 4 is also detected at the $8\sigma_I$ level of 0.6 mJy beam^{-1}: this detection is exceptional in a classic FRII source.

In the preceding lobe, the hotspot P1 shows unresolved, sub-kpc structure with fractional polarization exceeding ~ 40 per cent. Feature P2 is notably uniform in surface brightness with a ridge of enhanced fractional (~ 50 per cent) polarization around its western boundary and characteristically radial *E*-vectors.

The following lobe shows similar hotspot structure, though F1 is less compact than P1. F2 shows similar polarization structure to P2.

6 REVIEW

As indicated in the introduction, we attempt no detailed astrophysical interpretation of the maps in the present paper, and consideration of trends and correlations is deferred until the whole sample is available. Nevertheless, some striking features invite comment, and we draw attention to these here.

(i) No standard hotspot structure is prevalent. Even the two ends of the same source are often very different, though the structures and radio luminosities of the two lobes are generally similar (with obvious exceptions). This suggests that hotspots are not steady patterns but transient features, changing over time-scales short compared with that of the age of the source. [For example, the three-dimensional simulations by Cox *et al.* (1990) reveal unsteady hotspot structures changing on time-scales of one tenth to one hundredth of the source age – for a steadily precessing (short and broad) jet in a *uniform* ambient medium. For a real (long and narrow) jet propagating into a non-uniform medium, we would expect variations in hotspot structure on time-scales even shorter than these.]

(ii) When examined at high resolution, many sources do not show the canonical pattern of a compact ('primary') together with a less compact ('secondary') hotspot at each end. Indeed, some sources (e.g. 3C227, 403) have three or more hotspots at one end.

(iii) Long narrow features, like those generally called jets, appear in five of the eight sources, and perhaps also in 3C223.1 (Nf side); only in 3C197.1 and 227 are they not detected. It is well known that large-scale jets are common in quasars, but until now very few have been detected in FRII radio galaxies. Those found here are generally faint and require high sensitivity for detection against the lobe; if these properties are typical of those of jets in radio galaxies, it would explain why so few have been reported.

(iv) There is a very large difference in scale between the size of the whole source and the hotspot structures, exceeding 1000:1 in some cases (3C227, 452).

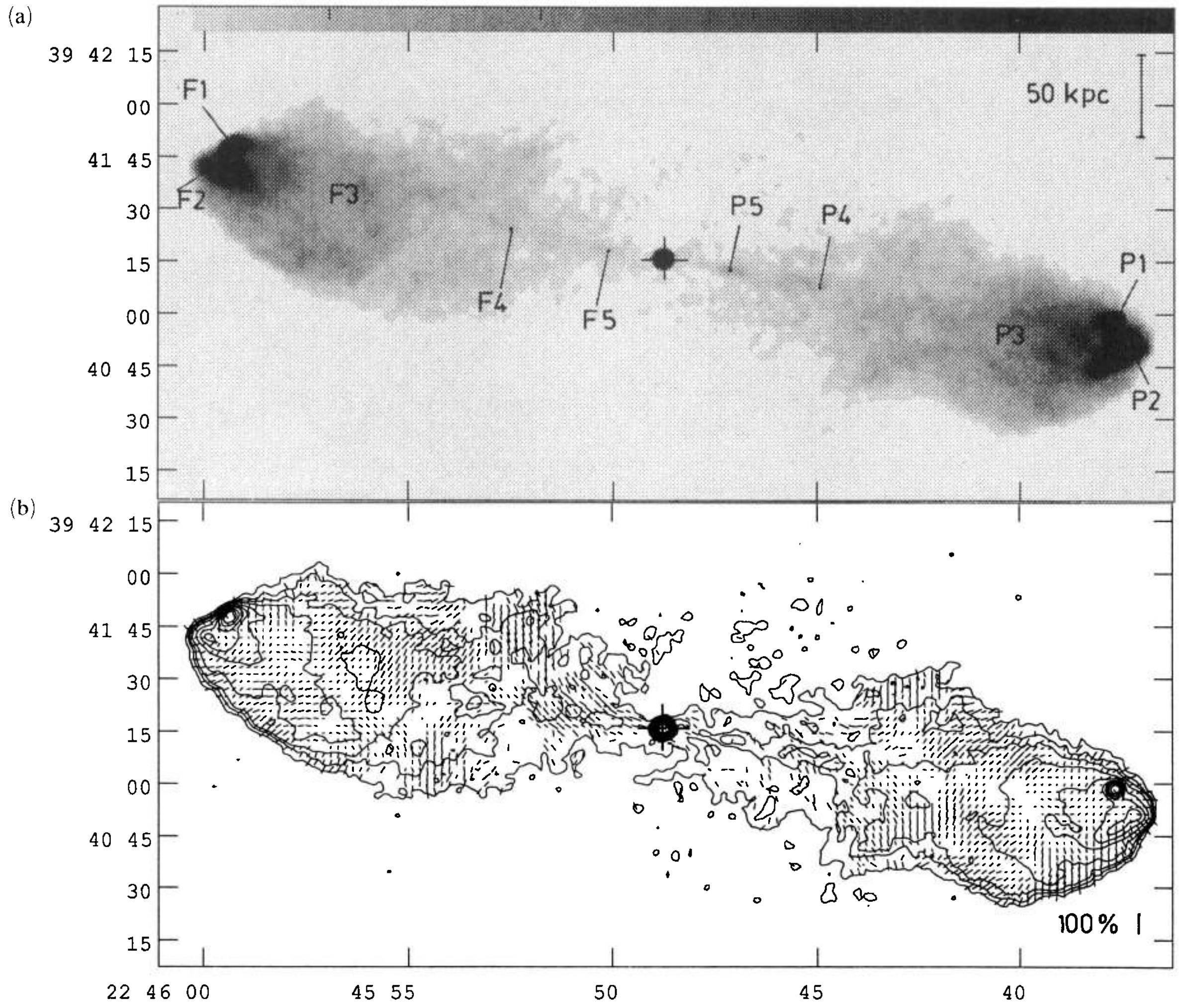

Figure 24. 3C452 at 2.5-arcsec resolution. (a) Grey-scales are shown for 0.2 mJy beam^{-1} (white) to 5 mJy beam^{-1} (black). (b) Contours are shown at (−4, 4, 8, 12, 20, 40, 70, 100, 150, 200, 300, 500, 800) × 75 μJy beam^{-1} and $\Delta\phi_8 \simeq -20°$.

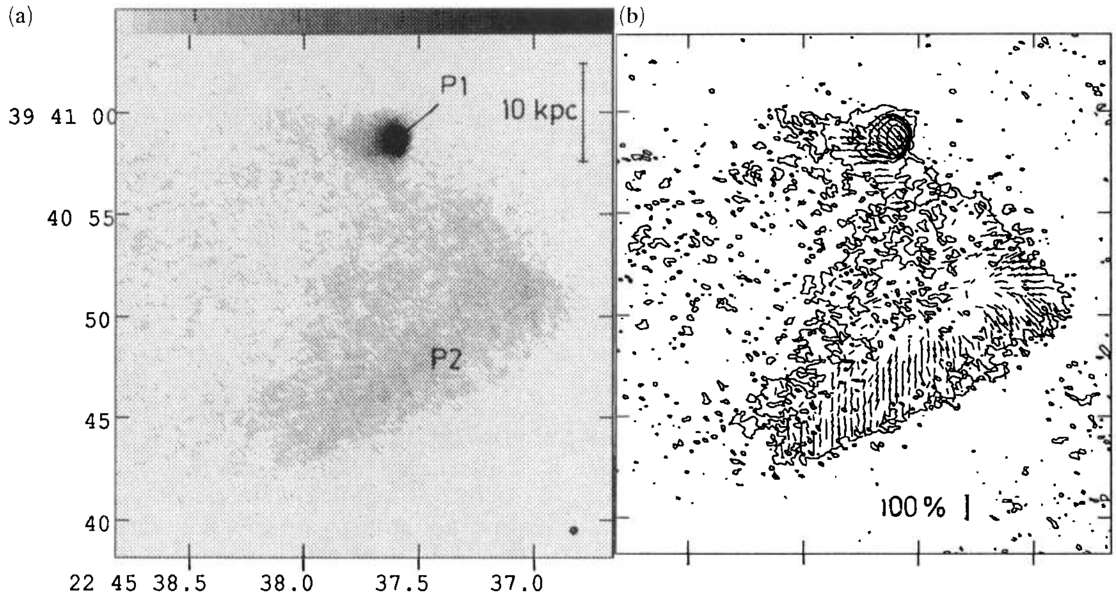

Figure 25. Hotspot in Sp lobe of 3C452 at 0.25-arcsec resolution. (a) Grey-scales are shown for 0.05 mJy beam^{-1} (white) to 1 mJy beam^{-1} (black). (b) Contours are shown at (−3, 3, 8, 12, 20, 40, 80) × 30 μJy beam^{-1} and $\Delta\phi_8 \simeq -20°$.

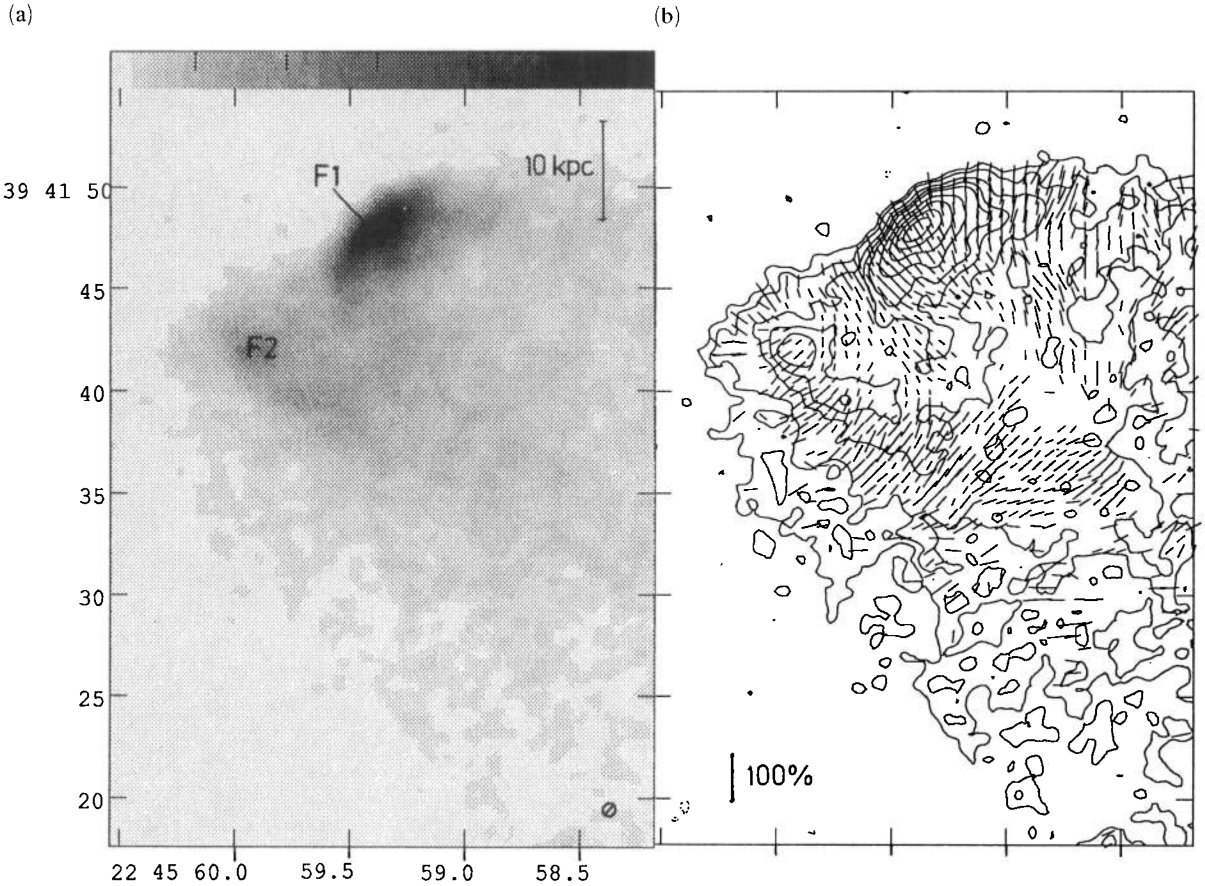

Figure 26. Hotspot in Nf lobe of 3C452 at 0.75-arcsec resolution. (a) Grey-scales are shown for 0.05 mJy beam^{-1} (white) to 3 mJy beam^{-1} (black). (b) Contours are shown at $(-3, 3, 5, 10, 15, 20, 30, 40, 50, 60) \times 50$ μJy beam^{-1} and $\Delta\phi_8 \simeq -20°$.

(v) Two of our eight sources (3C223.1 and 403) have large wings of low surface brightness, each at a position angle very different from that of the main source – this suggests that the central engine has undergone a drastic change in orientation at some time during the past 10^8 yr. The back-flow envisaged by Leahy & Williams (1984), channelled back into the old cavity of a former orientation, does not appear to explain how the wings could become longer than the main source. It is possible that 3C197.1 and 433 demonstrate a related phenomenon, though with a more recent change of direction.

(vi) A trend in the sample as a whole is that the more distorted and strikingly asymmetric sources are the smallest (often no bigger than the associated galaxy) while the simpler and more symmetric are the largest.

(vii) Some sources (e.g. 3C227) have lobes which widen and cut-off abruptly at straight boundaries on either side of the central core; in such sources the core then lies in a region with no detected emission. This structure is suggestive of a disc of central, dense, cold gas with its axis coincident with that of the source.

It is not yet clear whether these features are restricted to the lower power FRII sources of which the sample is predominantly composed, or whether they are more generally applicable to FRII sources of all luminosities.

ACKNOWLEDGMENTS

AB thanks the departments at NRAL and at the VLA for the use of their facilities. He also acknowledges support from the SERC. The VLA is part of the National Radio Astronomy Observatory and is operated by Associated Universities Inc., under cooperative agreement with the National Science Foundation.

REFERENCES

Baars, J. W. M., Genzel, R., Pauliny-Toth, I. I. K. & Witzel, A., 1977. *Astrophys. J.*, **61**, 99.
Begelman, M. C., Blandford, R. D. & Rees, M. J., 1984. *Rev. Mod. Phys.*, **56**, 255.
Burns, J. O., Christiansen, W. A. & Hough, D. H., 1982. *Astrophys. J.*, **257**, 538.
Carilli, C. L., 1990. PhD thesis, Massachusetts Institute of Technology.
Carilli, C. L., Dreher, J. W. & Perley, R. A., 1989. In: *Hotspots in Extragalactic Radio Sources*, p. 51, eds Meisenheimer, K. & Röser, H.-J., Springer-Verlag, Berlin.
Cornwell, T. J., 1989. In: *Synthesis Imaging in Radio Astronomy, ASP Conference Series No. 6*, p. 277, eds Perley, R. A., Schwab, F. R. & Bridle, A. H., Astronomical Society of the Pacific, San Francisco.
Cornwell, T. J. & Fomalont, E. B., 1989. In: *Synthesis Imaging in Radio Astronomy, ASP Conference Series No. 6*, p. 185, eds

Perley, R. A., Schwab, F. R. & Bridle, A. H., Astronomical Society of the Pacific, San Francisco.

Cox, C. L., Gull, S. F. & Scheuer, P. A. G., 1991. *Mon. Not. R. astr. Soc.*, **252**, 558.

Fanaroff, B. L. & Riley, J. M., 1974. *Mon. Not. R. astr. Soc.*, **167**, 31.

Kronberg, P. P., 1986. *Can. J. Phys.*, **64**, 449.

Laing, R. A., Riley, J. M. & Longair, M. S., 1983. *Mon. Not. R. astr. Soc.*, **204**, 151.

Leahy, J. P. & Williams, A. G., 1984. *Mon. Not. R. astr. Soc.*, **210**, 929.

Muxlow, T. W. B. & Garrington, S. T., 1991. In: *Beams and Jets in Astrophysics*, p. 69, ed. Hughes, P. A., Cambridge University Press, Cambridge.

Norman, M. L., 1989. In: *Hotspots in Extragalactic Radio Sources*, p. 193, eds Meisenheimer, K. & Röser, H.-J., Springer-Verlag, Berlin.

Rudnick, L., 1988. *Astrophys. J.*, **325**, 189.

Rudnick, L. & Anderson, M., 1990. *Astrophys. J.*, **355**, 427.

Scheuer, P. A. G., 1981. *Extragalactic Radio Sources: IAU Symp. No. 97*, p. 163, eds Heeschen, D. S. & Wade, C. M., Reidel, Dordrecht.

Simard-Normandin, M., Kronberg, P. P. & Button, S., 1981. *Astrophys. J. Suppl.*, **45**, 97.

Spinrad, H., Djorgovski, S., Marr, J. & Anguilar, L., 1985. *Publs astr. Soc. Pacif.*, **97**, 932.

van Breugel, W., Balick, B., Heckman, T., Miley, G. & Helfand, D., 1983. *Astrophys. J.*, **88**, 40.

van Breugel, W., Miley, G., Heckman, T., Butcher, H. & Bridle, A., 1985. *Astrophys. J.*, **290**, 496.

Williams, A. G. & Gull, S. F., 1985. *Nature*, **313**, 34.

Yates, M. G. & Longair, M. S., 1984. *Mon. Not. R. astr. Soc.*, **241**, 29.